

MODELING AND SIMULATION OF THE BOILING CRISIS
WITHIN PWR AT CFD SCALE

LUC FAVRE

Improving the Modeling of Wall Boiling for Multiphase CFD Simulations

Paris, December 2022

test

ABSTRACT

To write!

PUBLICATIONS

Some ideas and figures have appeared previously in the following publications:

Put your publications from the thesis here. The packages `multibib` or `bibtopic` etc. can be used to handle multiple different bibliographies in your document.

We have seen that computer programming is an art,
because it applies accumulated knowledge to the world,
because it requires skill and ingenuity, and especially
because it produces objects of beauty.

— knuth:1974 [knuth:1974]

ACKNOWLEDGEMENTS

Put your acknowledgements here.

Many thanks to everybody who already sent me a postcard!

Regarding the typography and other help, many thanks go to Marco Kuhlmann, Philipp Lehman, Lothar Schlesier, Jim Young, Lorenzo Pantieri and Enrico Gregorio¹, Jörg Sommer, Joachim Köstler, Daniel Gottschlag, Denis Aydin, Paride Legovini, Steffen Prochnow, Nicolas Repp, Hinrich Harms, Roland Winkler, and the whole L^AT_EX-community for support, ideas and some great software.

Regarding LyX: The LyX port was initially done by Nicholas Mariette in March 2009 and continued by Ivo Pletikosić in 2011. Thank you very much for your work and the contributions to the original style.

¹ Members of GuIT (Gruppo Italiano Utilizzatori di T_EX e L^AT_EX)

CONTENTS

I	INTRODUCTION	1
II	MODELING AND SIMULATION OF BOILING FLOWS USING CFD	2
1	NEPTUNE_CFD CODE	3
1.1	The NEPTUNE_CFD code and physical modeling	3
1.1.1	Simulation framework	3
1.1.2	Governing equations for turbulent boiling bubbly flows	3
1.1.3	Interfacial transfers closure laws	4
1.1.4	Turbulence modeling	5
1.1.5	Wall boiling model	5
1.1.6	Wall function for dispersed boiling flows	6
2	DEBORA CASES	8
2.1	Boiling freon in a simple tube : DEBORA experiments	8
2.1.1	Description of the experiment	8
2.1.2	NEPTUNE_CFD simulations of DEBORA cases	9
2.1.3	Investigating the nucleation site density modeling N_{sit}	10
III	DEVELOPMENT OF A NEW WALL HEAT FLUX PARTITIONING MODEL	12
3	EXISTING HEAT FLUX PARTITIONING MODELS	13
3.1	Kurul & Podowski (1990)	13
3.1.1	Basu (2000)	13
3.1.2	Yeoh (2006)	13
3.2	Gilman (2017)	13
3.3	Kommajosyula (2020)	13
4	BOILING BUBBLE DYNAMICS	14
4.1	Force Balance Modeling	14
4.1.1	General Considerations	14
4.1.2	Buoyancy and Body Forces	14
4.1.3	Capillary Force	14
4.1.4	Contact Pressure Force	15
4.1.5	Drag and Lift Forces	15
4.1.6	Added Mass Force	16
4.1.7	Force Balance Summary	18
4.1.8	Bubble Growth	18
4.1.9	Liquid Velocity	18
4.2	Departure by Sliding	19
4.2.1	Non-Dimensional Analysis	19
4.2.2	Low Pressure Data	20
4.2.3	High Pressure Data	21
4.2.4	Departure Diameter Prediction	21
4.3	Sliding phase	23
4.3.1	Modeling	23
4.3.2	Low Pressure Sliding	23
4.3.3	High Pressure	23
4.4	Conclusion	24
4.5	Establishment of the force balance for a bubble on a vertical wall	34
4.5.1	Bubble shape : Geometrical definitions	35

4.5.2 Buoyancy force	36
4.5.3 Contact Pressure force	37
4.5.4 Capillary force	37
4.5.5 Added Mass force of a growing bubble	37
4.5.6 Added Mass from Duhar <i>et al.</i>	41
4.5.7 Lift and drag forces	42
4.5.8 Dominant Forces at Departure by Sliding	44
4.5.9 Application to Low Pressure Data	46
4.5.10 Application to High Pressure Data	46
4.6 Prediction of bubble departure diameter	48
IV TOWARDS THE INDUSTRIAL GEOMETRY	50
5 PROMOTEUR	51
5.1 Boiling freon in a tube with mixing vanes : DEBORA-Promoteur experiments	51
5.1.1 Description of the experiment	51
5.1.2 NEPTUNE_CFD simulations of DEBORA-Promoteur cases	52
5.2 Liquid water flow in a tube with mixing vanes : AGATE-PROMOTEUR ex- periment	52
5.2.1 Description of the experiment	53
5.2.2 NEPTUNE_CFD simulations of AGATE-Promoteur case	53
V APPENDIX	55
A DETAILS ON THE BUBBLE FORCE BALANCE	56
A.1 Appendix Section Test	57
A.2 Another Appendix Section Test	57
BIBLIOGRAPHY	59

LIST OF FIGURES

Figure 2.1 NCFD (lines) vs. Exp. (circles) - T_L and T_w - Cases C8G2P26W16Te44.9, Te49.6, Te66.6 and Te70.3 - Simulations using two meshes M1 (coarse) and M2 (fine).	9
Figure 2.2 NCFD (lines) vs. Exp. (circles) - α , d_G and $U_{G,z}$ - Cases C30G2P26W16Te66.6 and Te70.6 - Simulations using two meshes M1 (coarse) and M2 (fine).	10
Figure 2.3 N_{sit} correlations of Lemmert & Chawla (left) and Hibiki & Ishii (right) vs. exp. data from literature. Operation pressures are displayed. $\pm 50\%$ error bars are drawn in black.	10
Figure 2.4 NCFD results for α , T_L and T_w using Lemmert & Chawla and Hibiki & Ishii correlation. Cases 8G2P26W23Te66.6 and Te70.3, 30G2P26W23Te66.6 and 70.6.	11
Figure 4.1 Sketch of the forces applied to the bubble facing an upward flow $\overline{U_L}$ and sliding at velocity $\overline{U_b}$	25
Figure 4.2 Drag correction from Shi <i>et al.</i> [Shi].	25
Figure 4.3 Dominance map regarding departure by sliding. Boundaries plotted for water at 1 bar and $D_d = 0.5\text{mm}$	26
Figure 4.4 Dominance map plotted for water at different pressures and bubble departure diameters.	27
Figure 4.5 Dominance map for R12 as simulating fluid for PWR. $D_d = 0.05\text{mm}$ is chosen according to R12 measurements from Garnier <i>et al.</i> [Garnier] who found bubbles of $\sim 0.1\text{mm}$ diameter after lift-off.	27
Figure 4.6 Dominance maps for each low pressure data sets.	28
Figure 4.7 Dominance map for high pressure measurements from Kossolapov . . .	28
Figure 4.8 D_d predictions using Eq. 4.34	29
Figure 4.9 D_d predictions using Eq. 4.35	29
Figure 4.10 D_d predictions using $d\theta = 4^\circ$ for Kossolapov	30
Figure 4.11 Bubble sliding velocity predictions on Maity cases	31
Figure 4.12 Bubble sliding length predictions on Kossolapov cases - $P = 20\text{ bar}$. .	32
Figure 4.13 Bubble sliding length predictions on Kossolapov cases - $P = 40\text{ bar}$. .	33
Figure 4.14 Bubble force balance in vertical flow boiling	34
Figure 4.15 Sketch of the supposed bubble shape with (right) and without inclination (left).	35
Figure 4.16 Representation of the shape functions	36
Figure 4.17 Force predominance map. Green, blue and black lines are respectively conditions (4.136), (4.137) and (4.138). Left represents $R = 0.25\text{ mm}$ for water at 1 Bar. Right represents $R = 0.05\text{ mm}$, water at 150 Bar (plain lines) and R12 at 25 Bar (dashed lines).	45
Figure 4.18 Experimental measurements in the dominance map. Plain lines correspond to Sugrue average departure radius (0.15 mm), dashed lines to Guan and Maity (0.59 mm).	47
Figure 4.19 Experimental measurements from Kossolapov in the dominance map. Frontiers are plotted for the average departure radius at the given pressure. Blue : 39.8 Bar - Green : 19.9 Bar - Red : 10.5 Bar.	48
Figure 4.20 Predicted diameter by Eq. 4.139 vs. experimental measurements. Colors refer to the dominant force at the departure by sliding (left) or to the operating pressure (right). $\pm 50\%$ error lines in dashed black.	49
Figure 5.1 Picture of the mixing device (left) and its fine meshing (right).	51

Figure 5.2	NCFD (lines) vs. Exp. (circles) - α profiles for two MV positions ($23.5D_h$ in blue, $10D_h$ in orange) - $T_{in} = 65^\circ\text{C}$ (left), $T_{in} = 69^\circ\text{C}$ (middle), $T_{in} = 75^\circ\text{C}$ (right) - Simulations using two meshes M1 (coarse) and M2 (fine) for $T_{in} = 69^\circ\text{C}$	52
Figure 5.3	NCFD vs. Exp. - Top & Middle : Radial velocity and turbulent RMS ($z = 30\text{mm}$ & $z = 440\text{mm}$) - Bottom : Axial velocity and turbulent RMS ($z = 440\text{mm}$).	54

LIST OF TABLES

Table 2.1	Water/R12 scaling (from Garnier <i>et al.</i> [Garnier2001], $D_h = 19.2\text{mm}$ for We)	8
Table 4.1	Summary of different force-balance mechanistic approaches	25
Table 4.2	Thermal-hydraulics parameters range for the low pressure data.	26
Table 4.3	Thermal-hydraulics parameters range for Kossolapov data.	26
Table 4.4	Variables used by Shi <i>et al.</i>	43
Table 4.5	Thermal-hydraulics parameters range for the low pressure data.	46
Table 4.6	Weber, Capillary and Eotvos numbers range for the low pressure data.	46
Table 4.7	Thermal-hydraulics parameters and dimensionless numbers range for Kossolapov data.	47
Table A.1	Autem usu id	58

LISTINGS

Listing A.1	A floating example (<code>listings</code> manual)	58
-------------	--	----

ACRONYMS

CFD Computational Fluid Dynamics

CMFD Computational Multi-Fluid Dynamics

NCFD NEPTUNE_CFD

DNS Direct Numerical Simulation

NSD Nucleation Site Density

NOMENCLATURE

$N_{sit,0}$ Nucleation Site Density computed by correlation [m⁻²]

Part I
INTRODUCTION

Part II

MODELING AND SIMULATION OF BOILING FLOWS USING CFD

1

NEPTUNE_CFD CODE

1.1 THE NEPTUNE_CFD CODE AND PHYSICAL MODELING

1.1.1 *Simulation framework*

NEPTUNE_CFD is an eulerian multiphase CFD solver co-developed by EDF, CEA, IRSN and Framatome mostly for nuclear reactor applications. The code consists of a local three-dimensional modeling based on a two-fluid one pressure approach combined with mass, momentum and energy conservation equations for each phase[**Guelfi2007**].

The constitutive equations are solved using a pressure correction, and is based on a finite-volume discretization along with a collocated arrangement of the variables. Moreover, NEPTUNE_CFD allows the use of all type of meshes (hexahedra, tetrahedra, pyramids, etc.), even non-conforming ones, thanks to its face-based data structure. Finally, the code is well-suited for parallel computing, widening its computing capacity to very large meshes.

1.1.2 *Governing equations for turbulent boiling bubbly flows*

To simulate two-phase dispersed boiling flows, NEPTUNE_CFD solves the ensemble-averaged equations of mass conservation, momentum balance and energy conservation for each phase (total of 6 equations) :

Mass conservation :

$$\frac{\partial \alpha_k \rho_k}{\partial t} + \bar{\nabla} \cdot (\alpha_k \rho_k \bar{U}_k) = \Gamma_k \quad (1.1)$$

Where α_k , ρ_k , \bar{U}_k are the time fraction, average density and velocity of phase k ; $\Gamma_k = \Gamma_{k,i} + \Gamma_{k,w}$ the interfacial mass transfer term per unit of volume and time splitted between bulk and wall contribution. Subscripts $k = L$ or G denotes the liquid or gas phase, i the interfacial quantities and w the wall contribution.

Momentum balance :

$$\frac{\partial \alpha_k \rho_k \bar{U}_k}{\partial t} + \bar{\nabla} \cdot (\alpha_k \rho_k \bar{U}_k \otimes \bar{U}_k) = -\alpha_k \bar{\nabla} (P) + \bar{F}_{k,i} + \Gamma_k \bar{U}_{k,i} + \alpha_k \rho_k \bar{g} + \bar{\nabla} \cdot (\alpha_k (\bar{\tau}_{k,m} + \bar{\tau}_{k,T})) \quad (1.2)$$

Where P is the pressure, \bar{g} the gravity, $\bar{F}_{k,i}$ the interfacial forces accounting for momentum transfer between phases per unit of volume and time, $\bar{U}_{k,i}$ the interfacial velocity, $\bar{\tau}_{k,m}$ and $\bar{\tau}_{k,T}$ respectively the viscous and turbulent (or Reynolds) stress tensor. Subscript m and T respectively denote the molecular (or laminar) and turbulent terms.

Energy conservation :

$$\begin{aligned} \frac{\partial \alpha_k \rho_k H_k}{\partial t} + \bar{\nabla} \cdot (\alpha_k \rho_k H_k \bar{U}_k) &= \frac{\partial \alpha_k P}{\partial t} + \Gamma_k H_{k,i} + \bar{F}_{k,i} \cdot \bar{U}_k + \bar{Q}_{k,I} + \bar{\nabla} \cdot (\alpha_k (\bar{\tau}_k + \bar{\tau}_{k,T}) \cdot \bar{U}_k) \\ &\quad + \bar{\nabla} \cdot (\alpha_k (-(\lambda_{k,m} + \lambda_{k,T}) \bar{\nabla} (T_k))) + \alpha_k \rho_k \bar{g} \cdot \bar{U}_k + \bar{Q}_{k,w} \end{aligned} \quad (1.3)$$

Where $H_k = e_k + \frac{U_k^2}{2} + \frac{P}{\rho_k} = h_k + \frac{U_k^2}{2}$ is the total enthalpy of phase k , $H_{k,i}$ the interfacial-averaged enthalpy, $Q_{k,i}$ the interfacial heat flux per unit of volume and time, $\lambda_{k,m}$ and $\lambda_{k,T}$ respectively being the laminar and turbulent thermal conductivity, T_k the temperature, $Q_{k,w}$ the heat flux from the wall to phase k per unit of volume and time.

However, this ensemble-average approach requires a given number of closure laws since this operation removes most of the information about smaller scales physics such as interfacial exchanges between phases or wall-fluid interaction. Terms for which this modeling effort is needed are colored in orange in equations 1.1, 1.2 and 1.3. The chosen expressions for those terms are detailed in subsections 1.1.3, 1.1.4 and 1.1.5.

1.1.3 Interfacial transfers closure laws

The interfacial transfers of mass, momentum and energy are respectively noted in equations 1.1, 1.2 and 1.3 : Γ_k , $\overline{F_{k,i}}$ and $Q_{k,i}$.

Heat and mass transfers :

The mass transfer term, can be written as : $\Gamma_{L,i} + \Gamma_{G,i} = 0$, $\Gamma_{L,w} + \Gamma_{G,w} = 0$ with $\Gamma_{G,w} \geq 0$ in the case of boiling flows. This finally gives $\Gamma_L = -\Gamma_G$.

The interfacial heat flux $Q_{k,i}$ can be rewritten in terms of interfacial area concentration a_i : $Q_{k,i} = q''_{k,i} a_i$. Neglecting the mechanical contribution compared to the thermal terms, the energy jump condition can then be expressed as :

$$\sum_{k=L,G} \left(\Gamma_{k,i} h_{k,i} + q''_{k,i} a_i \right) = 0 \quad (1.4)$$

The estimation of $h_{k,i}$ is not straightforward since it can either be supposed to be the saturation enthalpy of phase k at the system pressure (H1) or $h_{k,i}$ can be identified to the phase-averaged enthalpy (H2). In NEPTUNE_CFD, the assumption H2 is chosen, thus giving the bulk condensation rate :

$$\Gamma_{L,i} = \frac{a_i (q''_{L,i} + q''_{G,i})}{h_{G,sat} - h_{L,sat}} \quad (1.5)$$

The interfacial heat flux densities $q''_{k,i}$ and interfacial area concentration a_i are expressed as $q''_{k,i} = C_{k,i} (T_{sat}(P) - T_k)$ and $a_i = 6\alpha_G/d_G$, d_G being the gas phase Sauter mean bubble diameter. The interfacial area is computed using the transport equation of RUYER & SEILER[Ruyer2009].

For subcooled liquid, the following heat transfer coefficient is used [Manon2000]:

$$C_{L,i} = \frac{Nu_L \lambda_L}{d_G} \text{ and } Nu_L = 2 + 0.6 Re^{1/2} Pr_L^{1/3} \quad (1.6)$$

Where Re is the bubble Reynolds number $Re = ||\overline{U_G} - \overline{U_L}|| d_G / \nu_L$ and Pr_L the liquid Prandtl number $Pr_L = \nu_L / \eta_L$ with ν_L and η_L respectively being the liquid kinematic viscosity and thermal diffusivity.

On the other hand, if the liquid is overheated, the maximum of three heat transfer coefficients accounting for different heat transfer mechanisms is taken [Berne1983]:

$$C_{L,i} = \max (C_{L,i,1}; C_{L,i,2}; C_{L,i,3}) \quad (1.7)$$

With $C_{L,i,n} = \lambda_L Nu_{L,n} / d_G$ and :

$$Nu_1 = \sqrt{\frac{4}{\pi} Pe} ; Nu_2 = 2 ; Nu_3 = \frac{12}{\pi} Ja \quad (1.8)$$

where $Pe = ||\overline{U_G} - \overline{U_L}|| d_G / \eta_L$ is the Peclet number and $Ja = \rho_L c_{p,L} |T_{sat} - T_L| / (\rho_g h_{lg})$ the Jakob number, with h_{lg} the latent heat of vaporization. Those three Nusselt numbers

respectively correspond to convection heat transfer, stationnary conduction and transient conduction.

For the gas phase, a simple law that ensures that the vapor temperature remains close to the saturation temperature is used (which is expected for small bubbles, *e.g.* in a PWR) :

$$C_{G,i} a_i = \frac{\alpha_G \rho_v c_{p,G}}{t_c} \quad (1.9)$$

where $c_{p,G}$ is the gas heat capacity at constant pressure, and t_c a characteristic (relaxation) time given by the user (default value being $t_c = 0.01\text{s}$) .

Interfacial forces :

The interfacial momentum transfer (excluding transfer associated to transfer of mass Γ_k) is assumed to be composed of 4 different forces being the, drag D , the added mass AM , the lift L and the turbulent dispersion TD :

$$\overline{F_{k,i}} = \overline{F_{k,D}} + \overline{F_{k,AM}} + \overline{F_{k,L}} + \overline{F_{k,TD}} \quad (1.10)$$

The turbulent dispersion force $\overline{F_{k,TD}}$ originates from the averaging operation conducted on the three other forces' expressions, detailed in equations 1.11, 1.12, 1.13 and 1.14.

$$\overline{F_{G,D}} = -\overline{F_{L,D}} = -\frac{1}{8} a_i \rho_L C_D \left| \left| \overline{U_G} - \overline{U_L} \right| \right| (\overline{U_G} - \overline{U_L}) \quad (1.11)$$

$$\begin{aligned} \overline{F_{G,AM}} = -\overline{F_{L,AM}} &= -C_{AM} \frac{1 + 2\alpha_G}{1 - \alpha_G} \alpha_G \rho_L \\ &\times \left[\left(\frac{\partial \overline{U_G}}{\partial t} + \overline{\nabla}(\overline{U_G}) \cdot \overline{U_G} \right) - \left(\frac{\partial \overline{U_L}}{\partial t} + \overline{\nabla}(\overline{U_L}) \cdot \overline{U_L} \right) \right] \end{aligned} \quad (1.12)$$

$$\overline{F_{G,L}} = -\overline{F_{L,L}} = -C_L \alpha_G \rho_L (\overline{U_G} - \overline{U_L}) \wedge (\overline{\nabla} \wedge \overline{U_L}) \quad (1.13)$$

$$\overline{F_{G,TD}} = -\overline{F_{L,TD}} = -\frac{2}{3} \alpha_L \alpha_G C_{TD} \overline{\nabla}(\alpha_G) \quad (1.14)$$

with C_D , C_{AM} , C_L and C_{TD} the associated forces coefficients, respectively taken from ISHII[Ishii1967], ZUBER[Zuber1964], TOMIYAMA[Tomiyama2002] and the Generalized Turbulent Dispersion model (GTD) from LAVIEVILLE *et al.* [Lavieville2017].

1.1.4 *Turbulence modeling*

For bubbly flow simulations, only liquid phase turbulence is taken into account. The prescribed model is the Reynolds Stress Model (RSM) $R_{ij} - \varepsilon SSG$ from SPEZIALE, SARKAR and GATSKI[Speziale1991] adapted to two-phase boiling flows by MIMOUNI *et al.* [Mimouni2011].

1.1.5 *Wall boiling model*

The modeling of the heterogeneous boiling phenomenon at the wall is based on a Heat Flux Partitioning (HFP) model, inspired by KURUL & PODOWSKI original work[Kurul1990] who divided the wall heat flux density ϕ_w in three terms :

- A single phase convective heat flux $\phi_{c,L}$ heating the liquid through the fraction of the wall area unaffected by the vapor bubbles
- A vaporization heat flux ϕ_e which accounts for the generation of vapor through heterogeneous nucleation
- A quenching heat flux ϕ_q to represent the thermal impact of bubbles departing from the wall and being replaced by cool liquid

A fourth flux is added to this HFP in NEPTUNE_CFD, following MIMOUNI *et al.* [Mimouni2016] who consider a convective heat flux heating the vapour $\phi_{c,G}$ when the wall area is covered by a dense accumulation of bubbles.

The model thus gives Equation 1.15 :

$$\phi_w = \phi_{c,L} + \phi_e + \phi_q + \phi_{c,G} \quad (1.15)$$

The convective heat fluxes are expressed as $\phi_{c,k} = A_k h_{k,log} (T_w - T_k)$ with $h_{k,log} = \rho_k c_{p,k} u^* / T_L^+$; where A_k the fraction of the wall area facing phase k , T_w the wall temperature and $h_{k,log}$ the wall logarithmic convective heat transfer coefficient to phase k based on the wall functions for friction velocity u^* and non-dimensional liquid temperature T_L^+ described in 1.1.6.

The vaporization heat flux is computed following $\phi_e = N_{sit} f \rho_G h_{lg} \pi d_d^2 / 6$ with :

- N_{sit} the nucleation site density modeled as [Lemmert1977] : $N_{sit} = [210 (T_w - T_{sat})]^{1.8}$
- f the bubble detachment frequency expressed as [Cole1960] : $f = \sqrt{\frac{4}{3} \frac{g |\rho_v - \rho_l|}{\rho_l d_d}}$
- d_d the bubble detachment diameter given by Unal correlation [Unal1976] corrected by Borée *et al.* [ref] (Equation 1.16)

$$d_d = 2.42 \times 10^{-5} P^{0.709} \frac{a}{\sqrt{b\varphi}} \text{ with } a = \frac{(T_w - T_{sat}) \lambda_w}{2\rho_G h_{lg} \sqrt{\pi \eta_w}} \text{ and } b = \begin{cases} \frac{T_{sat} - T_L}{2(1 - \rho_G/\rho_L)}, & \text{if } St \leq 0.0065 \\ \frac{1}{2(1 - \rho_G/\rho_L)} \frac{\phi_{c,L} + \phi_e + \phi_q}{0.0065 \rho_L c_{p,L} ||\bar{U}_L||}, & \text{if } St > 0.0065 \end{cases} \quad (1.16)$$

where λ_w and η_w are the wall thermal conductivity and diffusivity, $St = \frac{\phi_{c,L} + \phi_e + \phi_q}{\rho_L c_{p,L} ||\bar{U}_L|| (T_{sat} - T_L)}$ is the Stanton number and $\varphi = \max \left(1; \left(\frac{||\bar{U}_L||}{U_0} \right)^{0.47} \right)$ with $U_0 = 0.61 \text{ m/s}$

Finally, the quenching heat flux follows the approach of DEL VALLE & KENNING [DelValle1985] supposing that it follows a semi-infinite transient conduction regime : $\phi_q = A_G t_q f \frac{2\lambda_L (T_w - T_L)}{\sqrt{\pi \eta_L t_q}}$ where t_q is the quenching time, supposed to be equal to $1/f$.

1.1.6 Wall function for dispersed boiling flows

In boiling flows, the formation of bubbles at the wall may disturb the liquid velocity profile in the boundary layer. To take this phenomena into account, MIMOUNI *et al.* [Mimouni2016] proposed a wall function for boiling flows which tends to the single-phase formulation when $\alpha_G \rightarrow 0$ and depends on the bubble diameter and density at the wall :

$$u^+ = \frac{1}{\kappa} \ln(y^+) + B - \Delta u^+ \text{ with } \Delta u^+ = \begin{cases} 0 & \text{if } k_r^+ \leq 11.3 \\ \frac{1}{\kappa} \ln(1 + C_{kr} k_r^+) & \text{if } k_r^+ > 11.3 \end{cases} \quad (1.17)$$

where $\kappa=0.41$ is the Von Karman constant, $B = 5.3$ the standard single-phase logarithmic law constant. Δu^+ represents the offset of u^+ due to the wall roughness induced by the presence of bubble. We have $C_{kr} = 0.5$ and $k_r = \frac{k_r \sqrt{u^* u_T}}{\nu_L}$ the "roughness Reynolds number" with $u_T = C_\mu^{1/4} \sqrt{k_L}$ defined from the $k - \varepsilon$ constant $C_\mu = 0.09$ and k_L the liquid turbulent kinetic energy. Finally, $k_r = \alpha_G d_G$.

The non-dimensional wall liquid temperature T_L^+ is modeled according to LEDUC [Leduc1995]:

$$T_L^+ = \begin{cases} Pr_L y^+, & \text{if } y^+ \leq 13.2 \\ 8.67 Pr_{L,T} \left(\frac{Pr_L}{Pr_{L,T}} - 1 \right) \left(\frac{Pr_{L,T}}{Pr_L} \right)^{0.25} + \frac{Pr_{L,T}}{\kappa} \ln(Ey^+) & \text{if } y^+ > 13.2 \end{cases} \quad (1.18)$$

With $Pr_{L,T} = 0.9$ the turbulent liquid Prandtl number, and $E = 7.76$ a constant for smooth walls.

2

DEBORA CASES

2.1 BOILING FREON IN A SIMPLE TUBE : DEBORA EXPERIMENTS

In this section, we simulate upward boiling flows of R12 in a vertical tube and compare the NEPTUNE_CFD (NCFD) results with experimental measurements conducted by CEA & EDF on the DEBORA test facility.

2.1.1 Description of the experiment

In the end of 1990's, CEA and EDF built a test facility called DEBORA which goal was to conduct series of experiments and measurements to establish a database for boiling flows of freon R12. The choice of freon is justified because of its use as a simulating fluid for water in PWR conditions (very close phase density ratio, Weber number We, Boiling number Bo and thermodynamic flow quality x_{eq}). Table 2.1 sums up the flow conditions scaling between R12 and water.

Table 2.1: Water/R12 scaling (from Garnier *et al.* [Garnier2001], $D_h = 19.2\text{mm}$ for We)

Fluid	Water	Freon R12
Pressure P (bar)	100 - 180	14 - 30
Mass velocity G ($\text{kg}/\text{m}^2/\text{s}$)	1000 - 5000	1000 - 5000
Wall heat flux ϕ_w (MW/m^2)	0.5 - 6	0.05 - 0.65
Thermodynamic flow quality x_{eq} (-)	(-0.4) - (+0.4)	(-0.4) - (+0.4)
Density ratio ρ_G/ρ_L (-)	0.08 - 0.25	0.07 - 0.22
Weber number We (-)	2374 - 368 579	3319 - 438 966
Boiling number Bo (-)	3.67×10^{-5} - 2.39×10^{-3}	2.65×10^{-5} - 1.74×10^{-3}

The DEBORA experiment consists of an upward subcooled boiling flow of R12 in a 4m length pipe uniformly heated over 3.5m with an hydraulic diameter $D_h = 19.2\text{mm}$. Measurements of void fraction (α), interfacial velocity (*i.e.* axial gas velocity $U_{g,z}$), bubble diameter (d_G), liquid temperature (T_L) and wall temperature (T_w) at the end of the heating length were conducted through different series of tests. Experimental apparatus is detailed in Garnier *et al.* [Garnier2001] and Manon[Manon2000].

Different test campaigns were conducted on this experimental setup, in particular :

- Campaign 2900 : measurements of α , $U_{g,z}$ and d_G using one optical probe
- Campaign 3000 : measurements of α , $U_{g,z}$ and d_G using two optical probes
- Campaign 800 : measurements of T_L and T_w using thermocouples

Each experimental case is named following this nomenclature : CccGgPppWwwTett with cc being the campaign number, g the inlet mass velocity (G), pp the outlet pressure (P),

with the total heat power applied (W) and t the inlet temperature (T_{in}). For instance, C8G3P26W23Te69 refers to the case from the campaign 800 with $G \approx 3000 \text{ kg/m}^2/\text{s}$, $P \approx 26 \text{ bar}$, $W \approx 23 \text{ kW}$ and $T_{in} \approx 69^\circ\text{C}$.

2.1.2 NEPTUNE_CFD simulations of DEBORA cases

In this work, we present the simulations of the following cases :

- C8G2P26W16Te44.9 and C8G2P26W16Te49.6 (single-phase flow)
- C8G2P26W16Te66.6 and C8G2P26W16Te70.3 (two-phase flow)
- C30G2P26W16Te66.6 and C30G2P26W16Te70.6 (two-phase flow)

The pressure of 26 bar is chosen to match the pressure of the mixing vanes cases (DEBORA-Promoteur, Section 5.1). Mesh sensitivity is performed over two meshes : a large mesh (M1) with 460 356 cells = 338 radial \times 1362 axial cells and a fine mesh (M2) with 3 157 952 cells = 1568 radial \times 2014 axial cells.

On Figure 2.1, we present the results regarding liquid temperature at the outlet and wall temperature. The liquid temperature profile seems to be correctly reproduced by the simulations, though we see a slight overestimation close to the wall. Looking closer at boiling cases shows a difference of $\approx 0.5^\circ\text{C}$, which is close to the uncertainty of the measurements [Garnier2001]. Concerning the wall temperature, it appears that it is underestimated before the **Onset of Nucleate Boiling** (ONB) ($T_w < T_{sat}$) and overestimated after the ONB ($\approx +5^\circ\text{C}$). Post-ONB wall temperature is characterized by a stabilization of its value above the saturation temperature (here $T_{w,ONB} - T_{sat} \approx 2^\circ\text{C}$).

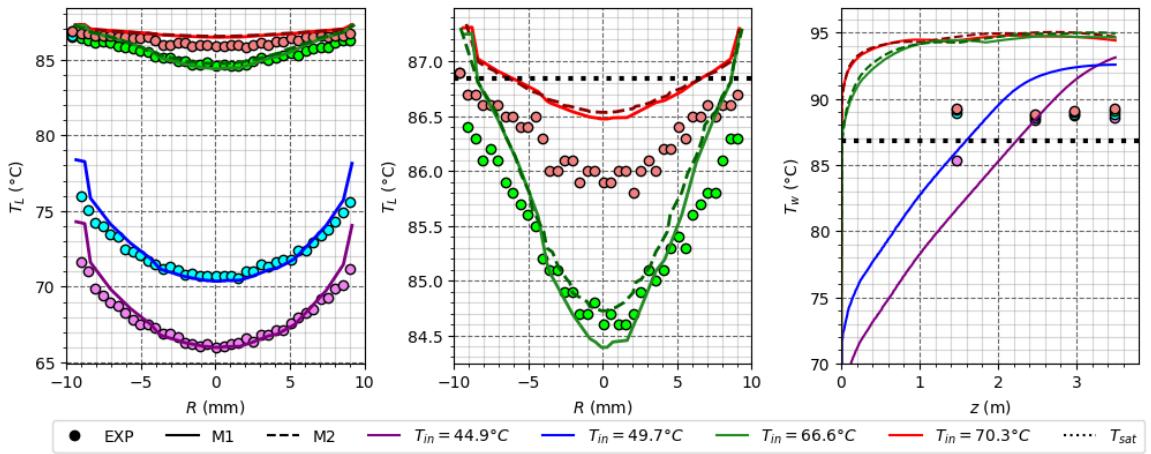


Figure 2.1: NCFD (lines) vs. Exp. (circles) - T_L and T_w - Cases C8G2P26W16Te44.9, Te49.6, Te66.6 and Te70.3 - Simulations using two meshes M1 (coarse) and M2 (fine).

On Figure 2.2, we compare the results of the simulations to the experiments regarding void fraction, bubble Sauter diameter and axial gas velocity. Void fraction profiles are quite correctly reproduced, though we observe a 10% higher peak at the wall for $T_{in} = 66.6^\circ\text{C}$. The order of magnitude of bubble diameter is correct ($\sim 0.1\text{mm}$) and NEPTUNE_CFD manages to detect coalescence (increase of bubble diameter when leaving the wall) and bulk condensation (decrease of bubble diameter when reaching the core of the flow), which is in qualitative agreement with the experiments. Quantitatively speaking, bubble diameter is globally underestimated. Finally, gas velocity profile is reasonably reproduced for $T_{in} = 66.6^\circ\text{C}$, but not for $T_{in} = 70.6^\circ\text{C}$. The latter experimental profile is flatter, which could be explained by a change of flow regime since uncondensed vapor is detected in the bulk.

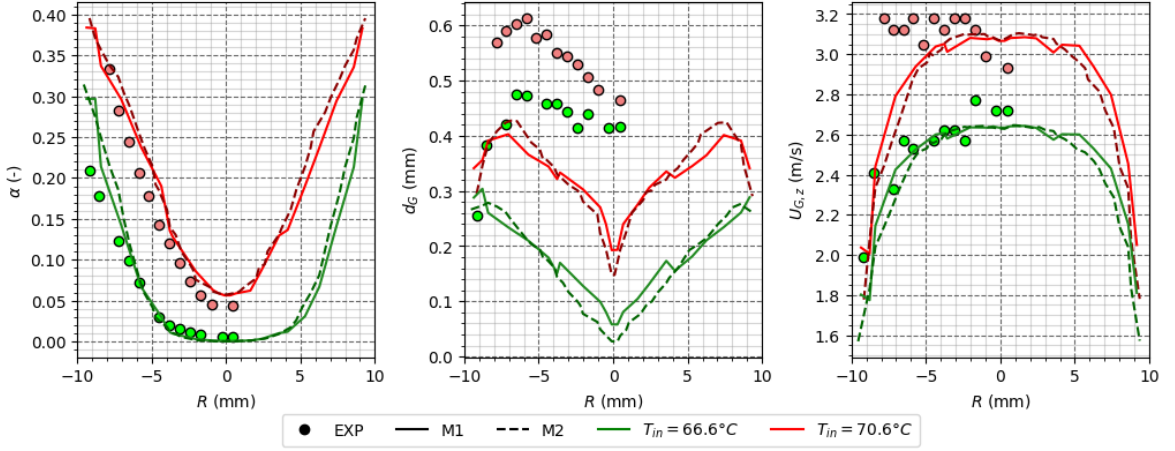


Figure 2.2: NCFD (lines) vs. Exp. (circles) - α , d_G and $U_{G,z}$ - Cases C30G2P26W16Te66.6 and Te70.6 - Simulations using two meshes M1 (coarse) and M2 (fine).

Finally, the simulations reasonably agree with the experiments. The strongest discrepancies being mostly the wall temperature and bubble diameter. Potential ways of improving those results are investigated in next sub-section.

2.1.3 Investigating the nucleation site density modeling N_{sit}

In NEPTUNE_CFD, wall temperature is computed through the Heat Flux Partitioning model, which role is to find the appropriate T_w which balances Equation 1.15. However, some laws used to express parameters such as N_{sit} , f , or d_d are quite old and simple. For instance, the Lemmert & Chawla [Lemmert1977] expression of N_{sit} only depends on the wall superheat (Sub-section 1.1.5).

A comparison of the Lemmert & Chawla law [Lemmert1977] with the Hibiki & Ishii [Hibiki2003] law for N_{sit} against 4 data sets from the literature is presentend on Figure 2.3. The Hibiki & Ishii correlation depends simultaneously on wall superheat, pressure and contact angle. Experimental measurements of Borishanskii *et al.* [Borishanskii1961], Richenderfer *et al.* [Richenderfer2018], Kossolapov *et al.* [Kossolapov2020] and Zhou *et al.* [Zhou2020] are used to assess the two nucleation site density correlations.

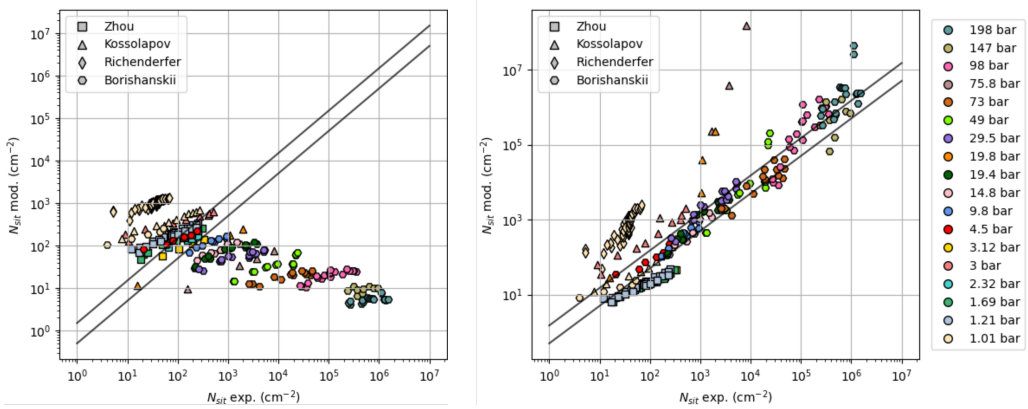


Figure 2.3: N_{sit} correlations of Lemmert & Chawla (left) and Hibiki & Ishii (right) vs. exp. data from literature. Operation pressures are displayed. $\pm 50\%$ error bars are drawn in black.

Figure 2.3 clearly shows that the Lemmert & Chawla law lack of pressure dependence fails to reproduce high pressure measurements contrary to the Hibiki & Ishii one. Even though Hibiki & Ishii correlation shows significant discrepancies with measurements of Kossolapov *et al.* and Richenderfer *et al.*, its prediction capability is greater in average than Lemmert & Chawla correlation.

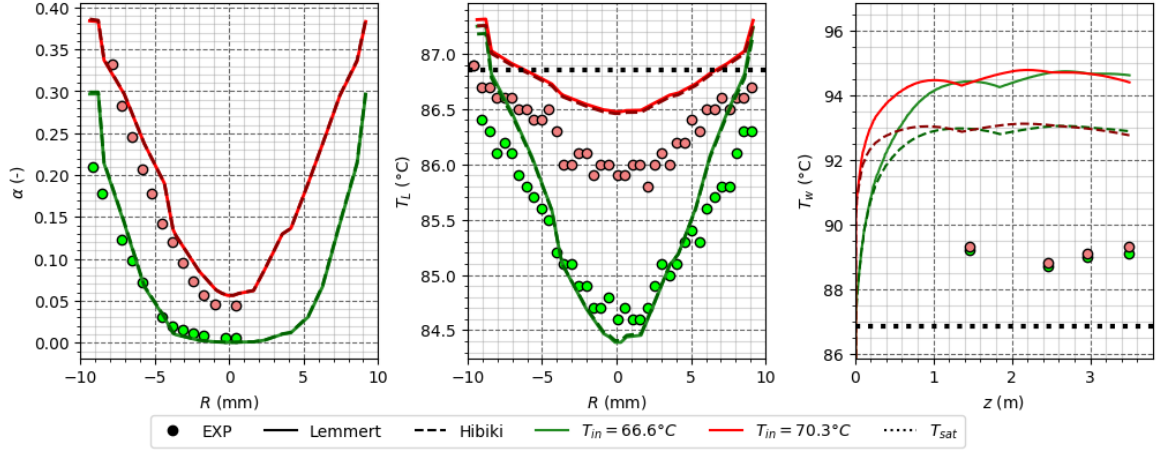


Figure 2.4: NCDF results for α , T_L and T_w using Lemmert & Chawla and Hibiki & Ishii correlation. Cases 8G2P26W23Te66.6 and Te70.3, 30G2P26W23Te66.6 and 70.6.

To assess the influence of nucleation site density law on NEPTUNE_CFD computations, we compare results obtained with both correlations on Figure 2.4, which shows a remarkable impact of the modification of N_{sit} correlation. Using Hibiki & Ishii correlation reduces the error on T_w by approximately 2°C while α and T_L remain unchanged. This implies that the same heat flux partitioning is found with the two models, but that the pressure dependence of Hibiki & Ishii law helped to balance Equation 1.15 using a lower T_w , thus closer to experimental measurements.

Such a result indicates that the HFP model could be improved through a systematic analysis of each parameter's impact and modeling (bubble departure diameter, detachment frequency, etc.). Assembling a more recent and consistent model could provide better results regarding wall temperature prediction. Models such as the one developed by Kommajosyula [Kommajosyula2020] could be interesting to apply for high-pressure flows.

Now that simple tube boiling flow has been assessed through the presented results, next section will focus on the simulation of boiling flow in a tube equipped with a mixing device.

Part III

DEVELOPMENT OF A NEW WALL HEAT FLUX PARTITIONING MODEL

3

EXISTING HEAT FLUX PARTITIONING MODELS

3.1 KURUL & PODOWSKI (1990)

In their original work published in 1990, Kurul & Podowski proposed a first complete closure for the wall heat flux partition.

They considered the applied heat flux to be divided between three mechanisms :

- A liquid single-phase heat flux $\phi_{c,l}$;
- A boiling heat flux ϕ_e to represent phase change from liquid to vapor ;
- A quenching heat flux ϕ_q to represent the effect of a bubble leaving the wall and being replaced by cold liquid.

The total wall heat flux being thus expressed as :

$$\phi_w = \phi_{c,l} + \phi_e + \phi_q \quad (3.1)$$

Each flux being expressed as follows :

$$\phi_{c,l} = A_{c,l} \rho_l c_{p,l} U_{l,\delta} \text{St}_{l,\delta} (T_w - T_{l,\delta}) \quad (3.2)$$

$$\phi_e = \frac{1}{6} \pi D_b^3 \rho_v h_{lv} f N_{sit} \quad (3.3)$$

$$\phi_q = t_q f A_q \frac{2\lambda_l (T_w - T_{l,\delta})}{\sqrt{\pi \eta_l t_q}} \quad (3.4)$$

3.1.1 Basu (2000)

Content

3.1.2 Yeoh (2006)

Content

3.2 GILMAN (2017)

Content

3.3 KOMMAJOSYULA (2020)

4

BOILING BUBBLE DYNAMICS

4.1 FORCE BALANCE MODELING

4.1.1 General Considerations

When trying to derive the force balance over a bubble, the first step consists of splitting the whole effort experienced by the bubble between different contributions depending on their nature. In our case, we focus on a bubble growing on a vertical wall and facing an upward flow as depicted in Figure 4.1. The considered forces are :

- The sum of the Buoyancy and Body forces $\overline{F_B}$;
- The Capillary or Surface Tension force $\overline{F_C}$;
- The Contact Pressure force $\overline{F_{CP}}$;
- The Drag and Lift forces $\overline{F_D}$ and $\overline{F_L}$;
- The Added-Mass force $\overline{F_{AM}}$.

Regarding the bubble shape, we consider a quasi-spherical bubble of radius R with a circular contact area with the wall of radius r_w . It has a static contact angle θ and is tilted under the influence of the flow by an inclination angle $d\theta$ (half the total angle hysteresis). The resulting downstream and upstream contact angles are therefore $\theta_d = \theta - d\theta$ and $\theta_u = \theta + d\theta$. If the bubble has a shape close to a truncated sphere, we can approximate the bubble foot radius as :

$$r_w \approx \frac{1}{2}R(\sin(\theta_u) + \sin(\theta_d)) = R \sin(\theta) \cos(d\theta) \quad (4.1)$$

We suppose $V_b \approx \frac{4}{3}\pi R^3$ for the bubble volume.

4.1.2 Buoyancy and Body Forces

The sum of the Buoyancy and Body forces results from both the weight of the bubble and the integration of the static liquid pressure over its surface which naturally yields :

$$\overline{F_B} = V_b (\rho_V - \rho_L) \bar{g} = \frac{4}{3}\pi R^3 (\rho_L - \rho_V) g \overline{e_x} \quad (4.2)$$

4.1.3 Capillary Force

The most common and generally accepted expression of the capillary force has been derived by Klausner[cite K1] by integrating the tangential effort at the triple contact line over the bubble foot radius while assuming an evolution of the contact angle from θ_d to θ_u as a polynomial expression of degree 3. This results in :

$$\begin{aligned}\overline{F_C} = & -\pi R \sigma \left[1.25 \frac{2d\theta}{(\frac{\pi}{2})^2 - d\theta^2} \sin(\theta)^2 \cos(d\theta)^2 \right] \overline{e_x} \\ & - \pi R \sigma \left[2 \sin(\theta)^2 \frac{\sin(2d\theta)}{2d\theta} \right] \overline{e_y}\end{aligned}\quad (4.3)$$

4.1.4 Contact Pressure Force

The Contact Pressure force originates from the pressure jump at the liquid-vapor interface exerted over the wall contact area and can be expressed using Laplace's equation as :

$$\overline{F_{CP}} \approx \frac{2\sigma}{R_c} \pi r_w^2 \overline{e_y} \approx \pi R \sigma 2 \sin(\theta)^2 \cos(d\theta)^2 \overline{e_y} \quad (4.4)$$

Here, R_c is the curvature radius of the bubble which is often assumed to be equal to $5R$ [Klausner, Sugrue, Mazzocco] without specific justification. To avoid this arbitrary choice, following the hypothesis of a nearly spherical bubble shape gives $R_c = R$.

4.1.5 Drag and Lift Forces

The external liquid flow over the bubble induces the well-known Drag and Lift forces which are usually computed using associated coefficients C_D and C_L defined by :

$$\overline{F_D} = \frac{1}{2} C_D \rho_L S_p (\overline{U_L} - \overline{U_b}) \|\overline{U_L} - \overline{U_b}\| \quad (4.5)$$

$$\overline{F_L} = \frac{1}{2} C_L \rho_L S_p (\overline{U_L} - \overline{U_b})^2 \overline{e_y} \quad (4.6)$$

with $S_p = \pi R^2$ the projected area of the bubble in the direction of the flow.

Traditional approaches rely on expressions of the Drag derived from the potential flow around the bubble[Duhar] or based on numerical correlations[Mei]. For instance, Mazzocco *et al.* [Mazzocco] use an expression of the Drag for a solid particle near a wall in a shear flow[Zeng] multiplied by a correction factor to account for the difference between a particle and a bubble. In this work, we propose to rely on the recent work of Shi *et al.* [Shi] who conducted Direct Numerical Simulations of a shear flow over a spherical bubble of constant radius close to a wall for bubble Reynolds number between 10^{-1} and 10^3 .

They computed the resulting Drag and Lift coefficients for each simulations and proposed correlations fitting their numerical results. The Drag coefficient is expressed as a correction of the Drag coefficient for a bubble in an unbounder uniform flow $C_{D,U}$. The total drag is given by :

$$C_D = (1 + \Delta C_D) C_{D,U} \quad (4.7)$$

where ΔC_D accounts for both the effect of the shear and the wall.

To cover the whole range of bubble Reynolds numbers, correlations at low and high Re_b are smoothly connected using an exponential term.

$$\Delta C_D = \Delta C_{D,Re_b=O(1)} + \left(1 - e^{-0.07 Re_b} \right) \Delta C_{D,Re_b \gg 1} \quad (4.8)$$

Each of those correction is computed depending on Re_b , the non-dimensional shear rate $Sr = \frac{\gamma^{2R}}{|U_{rel}|}$, the non dimensional distances $L_R = \frac{y}{R}$ and $L_u = y \frac{|U_{rel}|}{\nu_L}$ ($L_R = 1$ being a spherical bubble laying on a wall).

$$\Delta C_{D,\text{Re}_b=O(1)} = \frac{1 + \tanh(0.012\text{Re}_b^{0.8}) + \tanh(0.07\text{Re}_b^{0.8})^2}{1 + 0.16L_u(L_u + 4)} \times \left[\left(\frac{3}{8}L_R^{-1} + \frac{3}{64}L_R^{-4} \right) \left(1 - \frac{3}{8}L_R^{-1} - \frac{3}{64}L_R^{-4} \right)^{-1} - \frac{1}{16} \left(L_R^{-2} + \frac{3}{8}L_R^{-3} \right) \text{Sr} \right] \quad (4.9)$$

$$\Delta C_{D,\text{Re}_b \gg 1} = 0.47L_R^{-4} + 0.0055L_R^{-6}\text{Re}_b^{3/4} + 0.002|\text{Sr}|^{1.9}\text{Re}_b + 0.05L_R^{-7/2}\text{Sr}\text{Re}_b^{1/3} \quad (4.10)$$

Figure 4.2 shows the evolution of the Drag correction ΔC_D against the bubble Reynolds number for different distances to the wall L_R and two values of Sr. We can see that as the distance between the wall and the bubble increases the Drag correction logically approaches zero and that increasing the shear rate Sr increases ΔC_D for higher values of Re_b .

Shi *et al.* [Shi] conducted DNS for wall distances down to $L_R = 1.5$. However, Scheiff *et al.* [Scheiff] compared the values obtained for $L_R = 1$ measured with Drag of bubbles sliding on a wall and observed a good agreement, which legitimates the use of this new Drag correlation by extending its application to the case of a bubble laying on a wall.

The chosen uniform drag coefficient $C_{D,U}$ is proposed by Mei *et al.* [Mei].

$$C_{D,U} = \frac{16}{\text{Re}_b} \left[1 + \left(\frac{8}{\text{Re}_b} + \frac{1}{2} \left(1 + \frac{3.315}{\sqrt{\text{Re}_b}} \right) \right)^{-1} \right] \quad (4.11)$$

Since this work focuses on the sliding, the total force balance will be studied along the x axis, parallel to the wall. Thus, we do not detail the whole expression of Shi *et al.* for C_L . For further work, it is though interesting to mention that their expression of C_L is based on the sum of three contributions (wall presence, shear and a coupled term) and changes sign when reaching negative values or Sr for instance.

4.1.6 Added Mass Force

Added Mass effects originates from the transient behavior of the bubble dynamics being :

- Bubble growth ;
- Freestream acceleration (not considered in this work) ;
- Bubble acceleration.

In previous Mechanistic Models, different approaches were considered. In particular, some authors have chosen to rely on the Rayleigh-Plesset Equation for a growing hemispherical bubble in a quiescent flow to obtain the reaction force from the liquid, oriented perpendicularly to the wall.

$$\overline{F_{AM,RPE}} = -\rho_L \pi R^2 \left[R \ddot{R} + \frac{3}{2} \dot{R}^2 \right] \overline{e_y} \quad (4.12)$$

Then, assuming an inclination angle θ_i , this force is projected along the x axis to obtain an Added Mass force parallel to the wall that hinders departure. The inclination angle value is often empirical and used for data fitting[Klausner, Mazzocco].

$$\overline{F_{AM,RPE}} = -\rho_L \pi R^2 \left[R \ddot{R} + \frac{3}{2} \dot{R}^2 \right] (\sin(\theta_i) \overline{e_x} + \cos(\theta_i) \overline{e_y}) \quad (4.13)$$

This approach is questionable on different aspects. First, the RPE assumes a moving boundary in a quiescent unbounded liquid, which is physically far from the real situation of a bubble growing on a wall in a boiling flow. Moreover, the subsequent projection along the different directions regarding an unknown angle is hardly reasonable if θ_i is chosen arbitrarily.

To tackle the Added Mass derivation in a proper way, we propose to follow the approach of Lamb[Lamb] (also presented by Milne Thomson[Milne] or Van Winjgaarden[Winjgaarden]). By solving the potential flow around a bubble and its image, we can obtain the total liquid kinetic energy E_L that corresponds to a situation where a bubble is at a given distance from a wall represented by the line normal to the line of centers of the bubbles).

Then, we can use Lagrange's equations to compute the resulting forces in each direction.

$$F_{AM,x} = -\frac{\partial}{\partial t} \left(\frac{\partial E_L}{\partial \dot{x}} \right) + \frac{\partial E_L}{\partial x} \quad (4.14)$$

$$F_{AM,y} = -\frac{\partial}{\partial t} \left(\frac{\partial E_L}{\partial \dot{y}} \right) + \frac{\partial E_L}{\partial y} \quad (4.15)$$

To express the liquid kinetic energy, we can rely on the work of Van Der Geld[Van Der Geld] who derived E_L in the case of a full or truncated spherical bubble laying on a wall and facing an uniform flow parallel to the wall of velocity U_L (Eq. 4.16). If the bubble slides at a velocity $U_b = \dot{x}$, it sees a liquid velocity $U_{rel} = U_L - \dot{x}$.

$$E_L = \frac{\rho_L V_b}{2} \left(\alpha \dot{y}^2 + \text{tr}(\beta) \dot{R}^2 + \psi \dot{R} \dot{y} + \alpha_2 (U_L - \dot{x})^2 \right) \quad (4.16)$$

where α , $\text{tr}(\beta)$, ψ and α_2 are polynomials of $R/y = 1/L_R$ derived by Van Der Geld for $1 < R/y < 2$ i.e. $0.5 < L_R < 1$.

Injecting E_L in Eq. 4.14 and 4.15 and computing the values for the sphere case ($y = R$) yields :

$$F_{AM,x} = \rho_L V_b \left[3C_{AM,x} \frac{\dot{R}}{R} U_{rel} - C_{AM,x} \frac{\partial U_b}{\partial t} \right] \quad (4.17)$$

with $C_{AM,x} \approx 0.636$.

$$F_{AM,y} = \rho_L V_b \left[-(3C_{AM,y1} + C_{AM,y2}) \frac{\dot{R}^2}{R} - C_{AM,y1} \ddot{R} + C_{AM,y3} \frac{U_{rel}^2}{R} \right] \quad (4.18)$$

with $C_{AM,y1} \approx 0.27$, $C_{AM,y2} \approx 0.326$ and $C_{AM,y3} \approx 8.77 \times 10^{-3}$.

Parallel to the wall, the coupled term $\frac{\dot{R}}{R} U_{rel}$ in Eq. 4.17 **promotes detachment and sliding** of the bubble if $U_{rel} > 0$ e.g. if the bubble is attached to its nucleation site. This clearly contradicts the aforementioned approach where solely projecting the RPE on both axes lead to an Added-Mass term related to bubble growth that only hinders the departure by sliding. On the other hand, some authors[Klausner, Thorncroft, Guan] both projected the RPE to obtain an asymmetric growth term opposed to departure while also accounting for a detaching term due to the interaction between the flow induced by bubble growth and the external flow.

Moreover, Eq. 4.18 exhibits a term induced by the relative velocity that acts as a lift force, which seems to rarely appear in other approaches.

Here we want to insist on the importance on conducting an approach as rigorous as possible when deriving those transient aspects of the force balance. Otherwise, some terms may

be missing and lead to contradictory physical conclusions. Although the proposed method has already been used in different works, we obtained revisited values of the Added Mass coefficients based on the derivation of the liquid kinetic energy by Van Der Geld.

In the spirit of avoiding to introduce extra empirical terms, we keep the Added Mass force as presented in Eq. 4.17 and 4.18. No projection of the y term along the x axis to account for asymmetric bubble growth is considered for the moment.

4.1.7 Force Balance Summary

On Table 4.1, we sum up some of the mentioned force balance approaches and their models.

4.1.8 Bubble Growth

The question of the bubble growth law during its lifetime including sliding is still an open question that aims to cover various types of heat transfer :

- Evaporation due to superheated liquid near the bubble base ;
- Evaporation of a liquid microlayer trapped between the base of the bubble and the wall ;
- Condensation on top of the bubble when it reaches subcooled liquid ;
- Convective heat transfer due to relative velocity between the bubble and the liquid.

To our knowledge, many authors that have been tackling this issue had to consider empirical or fitted parameters when trying to exhaustively account for all the above heat transfers. For instance, Zhou[Zhou] and Yoo[Yoo] have proposed growth models that consider all the previously mentioned mechanisms. However, to fully close their mathematical model, many empirical values were used such as :

- The ratio between the bubble projected area and the microlayer area $C = A_b / A_{ML}$;
- The fraction of bubble area facing subcooling liquid ;
- Value of coefficients in the condensation law[Levenspiel].

Moreover, those models postulate the existence of a microlayer contributing to the growth while recent numerical and experimental investigations showed that the bubble may as well grow with a microlayer or in a pure contact line regime depending on the operating conditions [Urbano, Bures, Kossolapov].

In order to assess the force modeling proposed before, we choose a simpler growth law derived from heat conduction in the superheated liquid layer[Plessset].

$$R(t) = K \alpha_w \sqrt{\eta_L t} \quad (4.19)$$

where K is an adjustable constant, with a value roughly around 2[Plessset, Zwick, Yun]. This type of bubble growth has been widely used, and showed good agreement with many experimental observations and is particularly valid for early growth stages or small bubbles at high pressure.

4.1.9 Liquid Velocity

To compute the liquid velocity and shear rate at bubble center height, we use the wall law of Reichardt[Reichardt].

$$U_L^+ = \frac{1}{\kappa} \ln(1 + \kappa y^+) + c \left(1 - e^{-y^+/\chi} + \frac{y^+}{\chi} e^{-y^+/3} \right) \quad (4.20)$$

$$U_L = U_L^+ U_\tau \quad (4.21)$$

with $\kappa = 0.41$, $\chi = 11$ and $c = 7.8$.

$$\frac{\partial U_L^+}{\partial y^+} = \frac{1}{1 + \kappa y^+} + \frac{c}{\chi} \left(e^{-y^+/\chi} + \left(1 - \frac{y^+}{3} \right) e^{-y^+/3} \right) \quad (4.22)$$

$$\frac{\partial U_L}{\partial y} = \gamma = \frac{U_\tau^2}{\nu_L} \frac{\partial U_L^+}{\partial y^+} \quad (4.23)$$

The friction velocity is computed using Mac Adams correlation[MacAdams].

$$U_\tau = \sqrt{\frac{\tau_w}{\nu_L}} \quad (4.24)$$

$$\tau_w = 0.018 \text{ Re}_{D_h}^{-0.182} \frac{G_L^2}{\rho_L} \quad (4.25)$$

4.2 DEPARTURE BY SLIDING

4.2.1 Non-Dimensional Analysis

Now that the force balance has been established, we can write it parallel to the wall before bubble departure by sliding *i.e.* $U_b = \frac{\partial U_b}{\partial t} = 0$.

$$-\pi R \sigma f_{C,x} + \frac{4}{3} \pi R^3 (\rho_L - \rho_V) g + \frac{1}{2} C_D \rho_L \pi R^2 U_L^2 + \frac{4}{3} \pi R^3 \rho_L 3 C_{AM,x} \frac{\dot{R}}{R} U_L = 0 \quad (4.26)$$

$$f_{C,x} = 2.5 \frac{d\theta}{(\pi/2)^2 - d\theta^2} \sin(\theta)^2 \cos(d\theta)^2 \quad (4.27)$$

with $f_{C,x} \rightarrow 0$ if $d\theta \rightarrow 0$.

We can note that the departure by sliding is promoted by the Buoyancy, the Drag and the Added Mass. Only the Capillary force keeps the bubble attached to its nucleation site.

Re-writing Eq. 4.26 in non-dimensional form by dividing the LHS by the Added Mass force yields :

$$-\frac{1}{2} \frac{f_{C,x}}{K^2 C_{AM,x}} \frac{1}{Ca} \frac{Pr_L}{Ja_w^2} + \frac{1}{3} \frac{1}{K^2 C_{AM,x}} \frac{Re_b}{Fr} \frac{Pr_L}{Ja_w^2} + \frac{1}{8} \frac{C_D}{K^2 C_{AM,x}} Re_b \frac{Pr}{Ja_w^2} + 1 = 0 \quad (4.28)$$

where we have the following non-dimensional numbers :

$$Re_b = \frac{2 R U_L}{\nu_L} ; Fr = \frac{\rho_L U_L^2}{(\rho_L - \rho_V) g R} ; We = \frac{\rho_L U_L^2 R}{\sigma} ; Eo = \frac{(\rho_L - \rho_V) g R^2}{\sigma} ;$$

$$Ja_w = \frac{(T_w - T_{sat}) \rho_L c_{P,L}}{\rho_V h_{LV}} ; Pr_L = \frac{\nu_L}{\eta_L} ; \frac{\dot{R}}{U_L} = \frac{K^2 Ja_w^2}{Pr Re_b} ; Ca = \frac{\mu_L U_L}{\sigma}$$

Eq. 4.28 exhibits terms that can be used to compare the magnitude of each detaching forces. We can obtain the following conditions :

$$\text{Added Mass greater than Drag if : } \frac{\text{Ja}_w^2}{\text{Pr}} > \frac{1}{8} \frac{C_D}{C_{AM,x}} \frac{1}{K^2} \text{Re}_b \quad (4.29)$$

$$\text{Added Mass greater than Buoyancy if : } \frac{\text{Ja}_w^2}{\text{Pr}} > \frac{1}{3} \frac{1}{C_{AM,x} K^2} \frac{\text{Re}_b}{\text{Fr}} \quad (4.30)$$

$$\text{Drag greater than Buoyancy if : } \text{Re}_b > \frac{16}{3} \frac{1}{C_D} \frac{\text{Eo}}{\text{Ca}} = \text{Re}_c \quad (4.31)$$

Those boundaries can be plotted on a $(\text{Ja}_w^2 / \text{Pr} ; \text{Re}_b)$ map for a given fluid and bubble diameter D . An example of such a map is presented on Figure 4.3. This allows to visualize the operating conditions under which each of the detaching forces will be dominant. Logically, Buoyancy dominates for low Re_b regimes contrary to Drag. Added Mass dominates when values of $\text{Ja}_w^2 / \text{Pr}_L$ are high *i.e.* when bubble grows rapidly.

4.2.1.1 Influence of Pressure

On Figure 4.4, we draw the dominance map for 3 different pressures and associated orders of magnitude of bubble departure diameter[Kocamustafaogullari].

The impact of pressure is mostly seen through the decrease of bubble departure diameter. As pressure increases, Buoyancy becomes less likely to dominate while Drag and Added Mass display much larger dominance zones. The competition between those two mainly relies on the competition between liquid flow velocity and wall superheat or heat flux.

4.2.1.2 Comparison between Fluids

On Figure 4.5, we compare the dominance zones for R12 at 26 bars and water at 155 bars. Moderately pressurized R12 (10 to 30 bars) has often been used as a simulating fluid to mimic water in PWR since it has the same density ratio and Weber number for instance. Assuming that the conservation of Weber and Boiling numbers may lead to similar bubble departure diameters, we can observe that the boundaries between the two fluids are very close. This qualitatively indicates that R12 shall present bubble departure by sliding mechanisms similar to what happens in PWR, which could confort the confidence one may have in extrapolating the observations done using the simulating fluid to industrial applications.

4.2.2 Low Pressure Data

Now we want to apply this non-dimensional approach to experimental measurement in order to determine the actual departure by sliding regimes. We chose 3 low pressure data sets of bubble departure diameter measurements in vertical flow boiling of water. The test conditions are summarized on Table 4.2.

In each case, we have measurements of the wall temperature which allows to precisely place the experimental point on the dominance map.

However, as explained before, we need a D_d value to plot the dominance zones. Since measured D_d vary significantly in each experiment, we draw the boundaries for the max. and min. D_d values. Then, placing the measurements on the map leads to Figure 4.6.

The conclusion is pretty straightforward : a vast majority of the data points are located in the Added Mass dominance zone, meaning that **the Added Mass force parallel to the wall is the main force triggering the departure by sliding**. Some points from Guan and Maity are between the boundaries for the min. and max. D_d , implying that for those bubbles Added Mass and Buoyancy were of similar magnitude when departure by sliding occurred.

4.2.3 High Pressure Data

Following the same approach, we place experimental measurements at 20 bar and 40 bar from Kossolapov[Kossolapov] on the associated dominance map. Experimental conditions are summed up on Table 4.3.

Contrary to low pressure measurements, Kossolapov data do not provide wall temperature measurements associated to departure diameters. Using the information of the wall heat flux value, we estimate ΔT_w using Frost & Dzakowic correlation[Frost].

$$\Delta T_w = \text{Pr}_{L,sat} \sqrt{\frac{8\sigma\phi_w T_{sat}}{\lambda_L \rho_V h_{LV}}} \quad (4.32)$$

which yields superheats roughly between 1K and 2K.

To cover the potential uncertainty about the estimation of ΔT_w , the points on the map are drawn with a uncertainty band from $\text{Ja}_w/10$ to $10 \times \text{Ja}_w$.

The resulting map is presented on Figure 4.7. We can see the immediate difference with low pressure measurements : **all points are clearly in the Drag dominant zone**, even when considering a large uncertainty over Ja_w . Points could reach the Added Mass / Drag boundary only for highest estimations of Ja_w at 20 bars.

This main difference in the dynamic regime when bubble departs by sliding arises from multiple effects :

- The decrease of ρ_L/ρ_V with pressure, thus reducing Ja_w and the impact of the detaching Added Mass term ;
- The higher liquid mass fluxes in Kossolapov experiments, increasing the impact of the Drag ;
- The decrease of D_d with pressure, reducing the magnitude of Buoyancy.

4.2.4 Departure Diameter Prediction

After qualitative non-dimensional analysis of different experimental measurements, we can try to use the force balance to predict the bubble departure diameter of those data sets.

We consider the non-dimensional force balance before departure.

$$C_{AM,x} K^2 \frac{\text{Ja}_w^2}{\text{Pr}_L} + \frac{1}{3} \frac{\text{Re}_b}{\text{Fr}} + \frac{1}{8} C_D \text{Re}_b = \frac{1}{2} \frac{f_{C,x}}{\text{Ca}} \quad (4.33)$$

Since we only have the capillary term hindering departure as a first approach, we can suppose that departure is reached when :

$$C_{AM,x} K^2 \frac{\text{Ja}_w^2}{\text{Pr}_L} + \frac{1}{3} \frac{\text{Re}_b}{\text{Fr}} + \frac{1}{8} C_D \text{Re}_b > \frac{1}{2} \frac{f_{C,x}}{\text{Ca}} \quad (4.34)$$

which is similar to saying that the total force balance becomes positive parallel to the wall.

Regarding the values of the contact angle and hysteresis, we use :

- $\theta = 49.5^\circ$ and $d\theta = 41.5^\circ$ for Sugrue data, which is the highest hysteresis measured in her experiments ;
- $\theta = 52.5^\circ$ and $d\theta = 22.5^\circ$ for Guan data, which is the average values observed in his work ;
- $\theta = 45.5^\circ$ and $d\theta = 7.5^\circ$ for Maity who measured the average contact angles for each bubble during its lifetime.

- $\theta = 23.6^\circ$ for Kossolapov data based on a picture of the bubble projected area and dry spot area at 10.5 bars, $d\theta = 1^\circ$ supposing small bubbles at high pressure are nearly not tilted.

This yields the resulting prediction on Figure 4.8. We have a significant dispersion of the results with strong underestimations of the bubble departure diameters, particularly at low pressure. This could be due to :

- An underestimation of the capillary term $f_{C,x}$ associated to contact angle measurements ;
- An overestimation of a detaching term ;
- A missing term hindering departure by sliding.

In the presented approach, the main unknown term would be the growth constant K that controls the Added Mass term. However, we can also speculate that the stronger deformability of bubbles at low pressure may induce a resistive term that blocks the departure by sliding. This point has partially been discussed when deriving the Added Mass term in Subsection 4.1.6. We pointed the fact that simpler approaches considering arbitrary tilting of the bubble to split the force resulting from RPE over both axes could be inaccurate. However, Klausner originally followed this approach to account for asymmetric growth of the bubble. If we wish to test a similar correction, we can rely on the growth terms found in the reassessed Added Mass force in Eq. 4.18. **To avoid using an arbitrary inclination angle**, we use $\theta_i = d\theta$ which represents the bubble tilt through its hysteresis as depicted in Figure 4.1.

We thus add a non-dimensional term derived from the projection of the bubble growth term of Eq. 4.18 on the x axis :

$$C_{AM,x} K^2 \frac{Ja_w^2}{Pr_L} + \frac{1}{3} \frac{Re_b}{Fr} + \frac{1}{8} C_D Re_b > \frac{1}{2} \frac{f_{C,x}}{Ca} + \frac{(2C_{AM,y1} + C_{AM,y2})}{3} \frac{K^4 Ja_w^4}{Pr_L^2 Re_b} \sin(d\theta) \quad (4.35)$$

This correction yields D_d predictions of Figure 4.9. The predictions are significantly improved for the low pressure measurements while they remain unchanged for the high pressure cases. This could be expected with the small Ja_w values reached.

On the other hand, both cases show nearly no variation in the predicted departure diameters for Kossolapov data. Suspecting that this originates from the very low value chosen for $d\theta$, we try a slightly higher value of $d\theta = 4^\circ$ as a sensitivity test.

Results on Figure 4.10 show that this higher value of $d\theta$ permits a better prediction of high pressure measurements. Moreover, we observe no impact of using the projected growth term of Equation 4.35.

However, Kossolapov specified in his work that defining the departure event at high pressure was complicated because of both the nearly zero Capillary force hindering departure and the fact that bubbles started to leave their nucleation site nearly instantly[Kossolapov].

Generally speaking, once we consider the projected term for low pressure measurements, the model achieves reasonable predictions and exhibits a coherent trend with pressure. Although those results may appear less precise than other existing mechanistic models[Klausner, Mazzocco], we want to insist that our approach was conducted using a reduced number of arbitrary / empirical constants. Usually, other models rely on calibrated values of r_w , θ_i , $d\theta$ or K , which helps to achieve better predictions on given data sets.

4.3 SLIDING PHASE

4.3.1 Modeling

After departure, bubbles slide over a distance l_{sl} which scales the impact of the sliding phenomenon over the wall heat transfer. Achieving good prediction of bubble sliding velocity is then important if one wishes to correctly quantify its impact.

Following the force balance framework presented in Section 4.1, we can write Newton's second law parallel to the wall for the sliding bubble.

$$\rho_V \frac{d(V_b U_b)}{dt} = -\pi R \sigma f_{C,x} + \frac{4}{3} \pi R^3 (\rho_L - \rho_V) g + \frac{1}{2} C_D \rho_L \pi R^2 U_L^2 + \frac{4}{3} \pi R^3 \rho_L \left[3C_{AM,x} \frac{\dot{R}}{R} U_{rel} - C_{AM,x} \frac{dU_b}{dt} \right] \quad (4.36)$$

This equation can be re-written to express the bubble acceleration.

$$\left(1 + \frac{\rho_L}{\rho_V} C_{AM,x} \right) \frac{dU_b}{dt} = \left(\frac{\rho_L}{\rho_V} - 1 \right) g + \frac{3}{8} \frac{C_D}{R} \frac{\rho_L}{\rho_V} (U_L - U_b) |U_L - U_b| + 3 \frac{\dot{R}}{R} \left[C_{AM,x} \frac{\rho_L}{\rho_V} (U_L - U_b) - U_b \right] - \frac{3}{4} \frac{\sigma}{\rho_V} \frac{f_{C,x}}{R^2} \quad (4.37)$$

Then, we numerically solve this equation from the moment when $R \geq R_d$ using a first order Euler scheme. Next sections compare obtained results against low and high pressure data.

4.3.2 Low Pressure Sliding

Maity[Maity] provided simultaneous measurements of bubble radius and velocity over time for three liquid mass fluxes in vertical boiling. To assess the validity of Eq. 4.37, we modify the growth constant K in order to roughly match experimental radius measurements. The goal is to verify if the force balance allows a good prediction of bubble velocity provided a correct bubble growth. The contact angles were kept the same as in 4.2.4 since Maity provided average values over the bubble lifetime.

Results are displayed on Figure 4.11. The model seems to fairly good predict bubble sliding velocity for the 3 cases. The moment of departure is a bit underestimated as previously observed (Figure 4.9).

The biggest discrepancy is observed for the case at $G_L = 143.8 \text{ kg/m}^2/\text{s}$. The slope of the velocity profile is close to the experiments, but the bubble reaches a nearly constant acceleration too rapidly which yields an approximately constant overestimation of 0.1 m/s. The $G_L = 239.6 \text{ kg/m}^2/\text{s}$ is well predicted regarding the velocity. However, the growth profile was difficult to match since measurements exhibit significant changes in growth regime after departure, which is probably due to the bubble being large enough to be impacted by the bulk flow. A finer model for bubble growth could be of interest here.

We can note that values of K between 0.5 and 1 were used to better fit the bubble radius time profile.

4.3.3 High Pressure

In his work, Kossolapov conducted measurements of radius and sliding length over thousands of individual bubbles and then provided the associated statistical distributions. To compare our model with his measurements, we took the upper and lower bounds of R and l_{sl} over time and plotted the associated bands of measured values as shown on Figure 4.12 and 4.13.

Comparisons were done for cases at 20 bar and 40 bar and 3 different values of G_L . The value of $d\theta$ for the simulations was kept really small (2° at 20 bar and 0.5° at 40 bar) since bubble tilt is supposed to reduce during sliding because the relative velocity regarding the liquid flow is diminishing. Moreover, higher pressure means smaller bubbles that are even more unlikely to present a significant contact angle hysteresis. We also want to mention that neglecting the capillary term in Eq. 4.37 had a minor impact over the results except that the bubble accelerates a little bit faster.

The obtained results are in good agreement both with the observed values of sliding length its evolution, which means bubble sliding velocity is well predicted for these cases.

On the other hand, we must note that high values of K were needed to match bubble growth measurements. This may be due to an underestimation of the wall superheat coming from Eq. 4.32.

4.4 CONCLUSION

In this work, we proposed a revisited force balance for a single bubble in an vertical upward boiling flow. A recent correlation for the Drag coefficient was used thanks to DNS results of Shi *et al.* and new values of the Added Mass coefficients were derived from the expression of the liquid kinetic energy in a potential flow around a bubble proposed by Van Der Geld.

This force balance also uses a limited amount of empirical variables to avoid data fitting and try to rely as much as possible on the derived expressions.

From this modeling, a non-dimensional approach was conducted to study the departure by sliding process and identify the main detaching forces at the moment of departure. A non-dimensional map was used to determine the operating conditions ranges for which each force is dominant. Using experimental measurements of bubble departure diameter, it was found that Added Mass was the main detaching force at low pressure while high pressure departure by sliding is dominated by the Drag.

This force balance was then used to predict bubble departure diameter values. A global underestimation was found which could be corrected at low pressure by including a bubble inclination term that partially projects the orthogonal Added Mass force associated to growth along the wall. The lack of precision compared to other existing models is likely due to the absence of fitting parameters such as the bubble foot radius, inclination angle or growth rate. However, the model showed an acceptable trend with pressure which can be considered as an encouraging feature regarding its generality.

Finally, bubble sliding simulations were conducted and compared with low and high pressure data. The results showed great agreement with measurements if an appropriate bubble growth is used. This indicates that the proposed modeling of the forces correctly captures the dynamics of sliding bubbles.

Further work shall be conducted on a clean modeling of the bubble growth by including effects such as condensation, microlayer evaporation and impact of the external liquid flow. Existing models rely on many empirical values which thus reduces their general applicability outside of their validation range. For instance, studies conducted by Zhou[Zhou] and Yoo[Yoo] could be used by enriching their modeling with finer results to get rid of data fitting. DNS results such as those of Legendre *et al.* [Legendre] could be of interest in that prospect.

Finally, the precise estimation of the contact angle and hysteresis remains a critical parameter to predict departure by sliding. Local measurements of those values and their evolution with operating conditions would be a very valuable information in that regard.

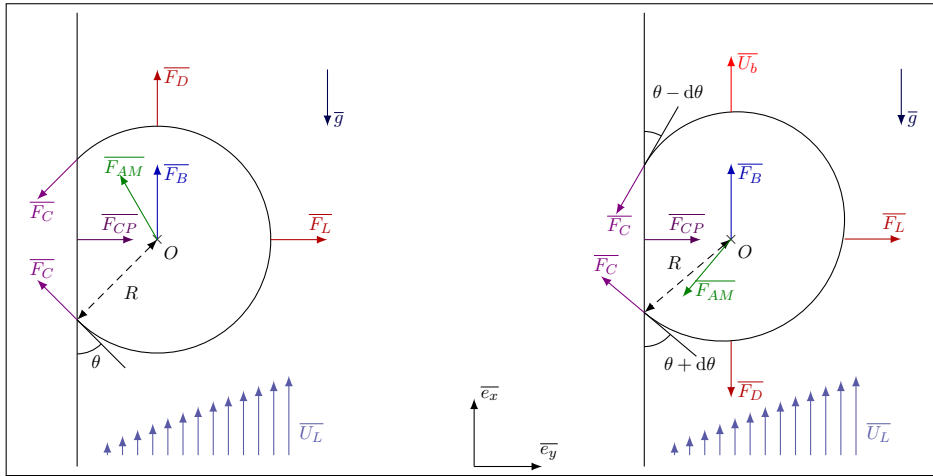


Figure 4.1: Sketch of the forces applied to the bubble facing an upward flow \bar{U}_L and sliding at velocity \bar{U}_b

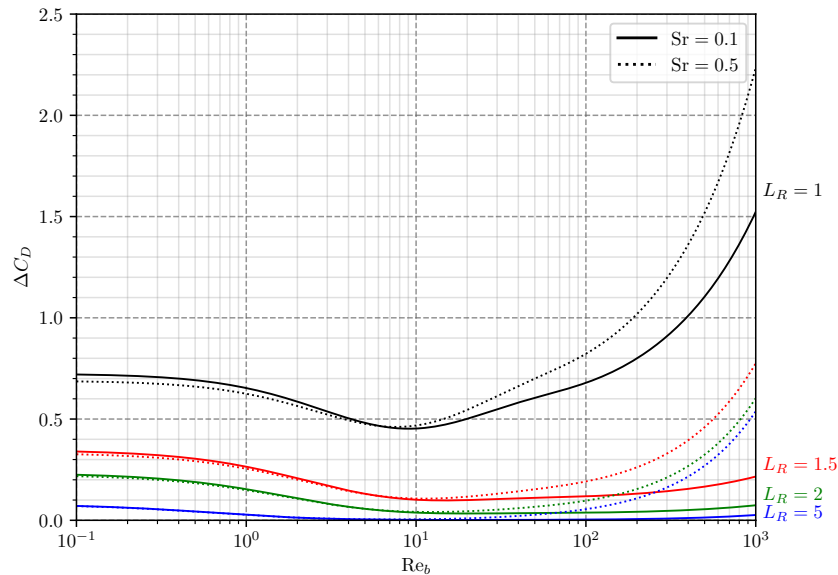


Figure 4.2: Drag correction from Shi et al. [Shi].

		Authors					
		Klausner	Thorncroft	Sugrue	Mazzocco	Ren	Present
Forces	\bar{F}_B	Eq. 4.2	Eq. 4.2	Eq. 4.2	Eq. 4.2	Eq. 4.2	Eq. 4.2
	\bar{F}_C	[Klausner]	[Klausner]	[Klausner]	[Klausner]	[Klausner]	[Klausner]
	\bar{F}_{CP}	Eq. 4.4	Eq. 4.4	Eq. 4.4	Eq. 4.4	Eq. 4.4	Eq. 4.4
	\bar{F}_D	[Mei]	[Mei]	[Mei]	[Zeng] × 0.66	[Mei]	[Shi] + [Mei]
	\bar{F}_L	a	a	a	a	a	[Shi]
	\bar{F}_{AM}	RPE, $\theta_i = \pi/17$	RPE, $\theta_i = \pi/17$	RPE, $\theta_i = \pi/17$	RPE, $\cos(\theta_i) = 1$, $\sin(\theta_i) = 0.2$	RPE, $\theta_i = \pi/17$	Potential flow [VdG] + Lagrange equation

Table 4.1: Summary of different force-balance mechanistic approaches

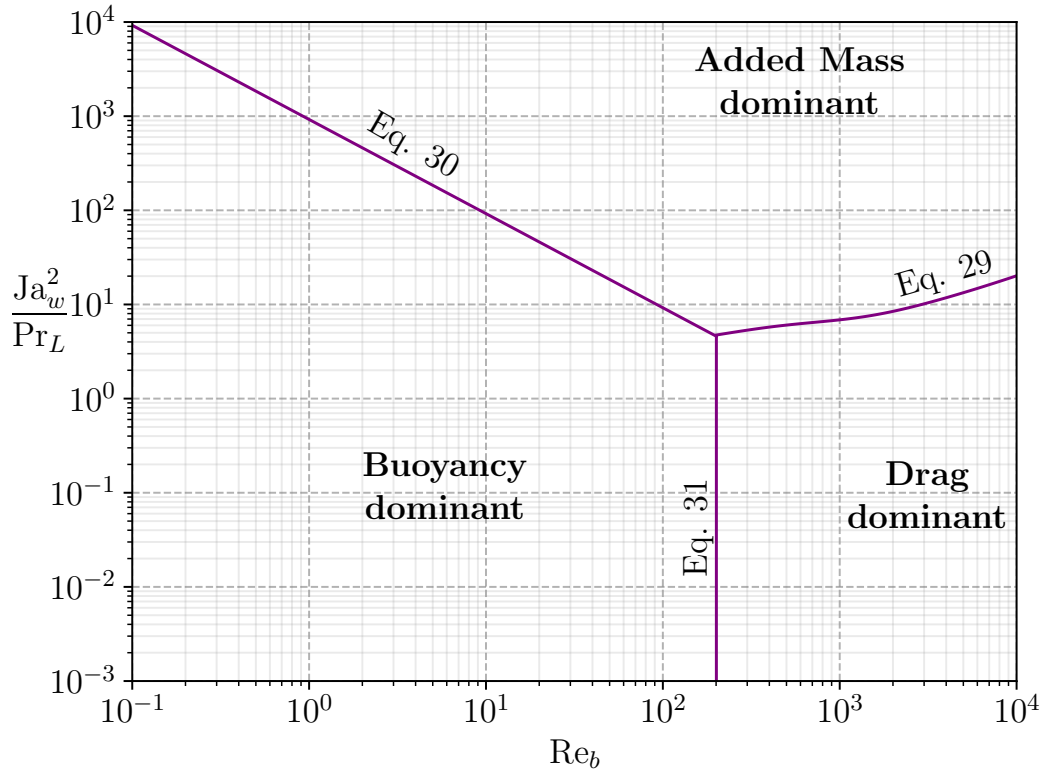


Figure 4.3: Dominance map regarding departure by sliding. Boundaries plotted for water at 1 bar and $D_d = 0.5\text{mm}$.

Author	D_h [mm]	G_L [$\text{kg}/\text{m}^2/\text{s}$]	ΔT_w [K]	D_d [mm]	Re_b (-)	Ja_w^2/\Pr (-)
Sugrue <i>et al.</i> [Sugrue]	16.642	250 - 400	2 - 6	0.229 - 0.391	139.1 - 180.1	20.57 - 185.2
Guan <i>et al.</i> [Guan]	9	87.3 - 319.2	4.5 - 8.5	0.62 - 1.85	193.3 - 923.4	104.2 - 371.6
Maity [Maity]	20	0 - 239.6	5 - 5.9	0.788 - 1.713	186.6 - 516.7	128.6 - 179.06

Table 4.2: Thermal-hydraulics parameters range for the low pressure data.

Author	D_h [mm]	G_L [$\text{kg}/\text{m}^2/\text{s}$]	P [Bar]	ϕ_w [$\text{MW} \cdot \text{m}^{-2}$]	D_d [mm]	Re_b [-]
Kossolapov[Kossolapov]	11.78	500-1500	19.9 39.8	0.178 - 0.495 0.291 - 0.613	0.021 - 0.047 0.01 - 0.035	43.9 - 110.2 17.0 - 55.9

Table 4.3: Thermal-hydraulics parameters range for Kossolapov data.

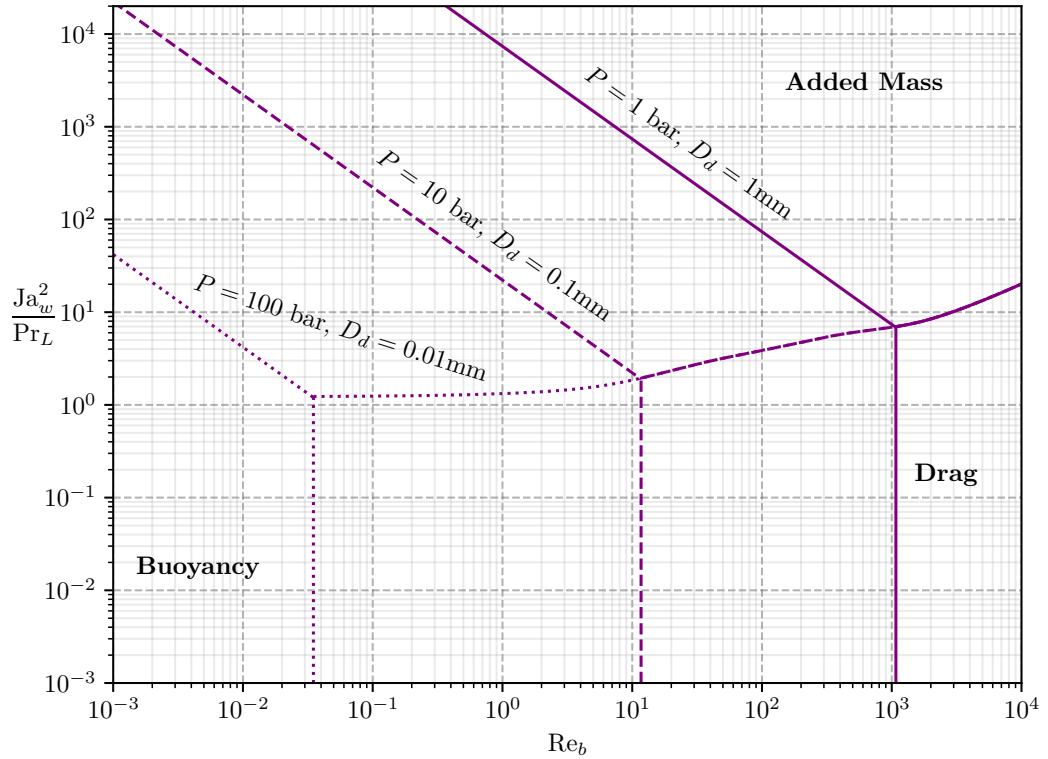


Figure 4.4: Dominance map plotted for water at different pressures and bubble departure diameters.

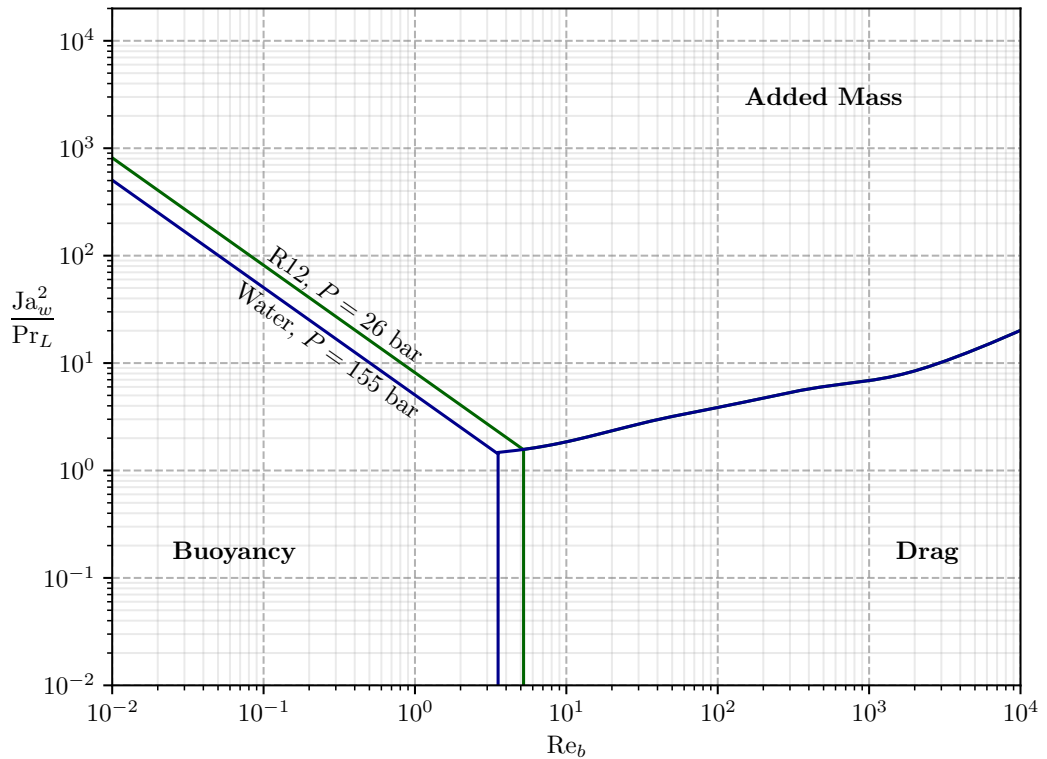


Figure 4.5: Dominance map for R12 as simulating fluid for PWR. $D_d = 0.05 \text{ mm}$ is chosen according to R12 measurements from Garnier *et al.* [Garnier] who found bubbles of $\sim 0.1 \text{ mm}$ diameter after lift-off.

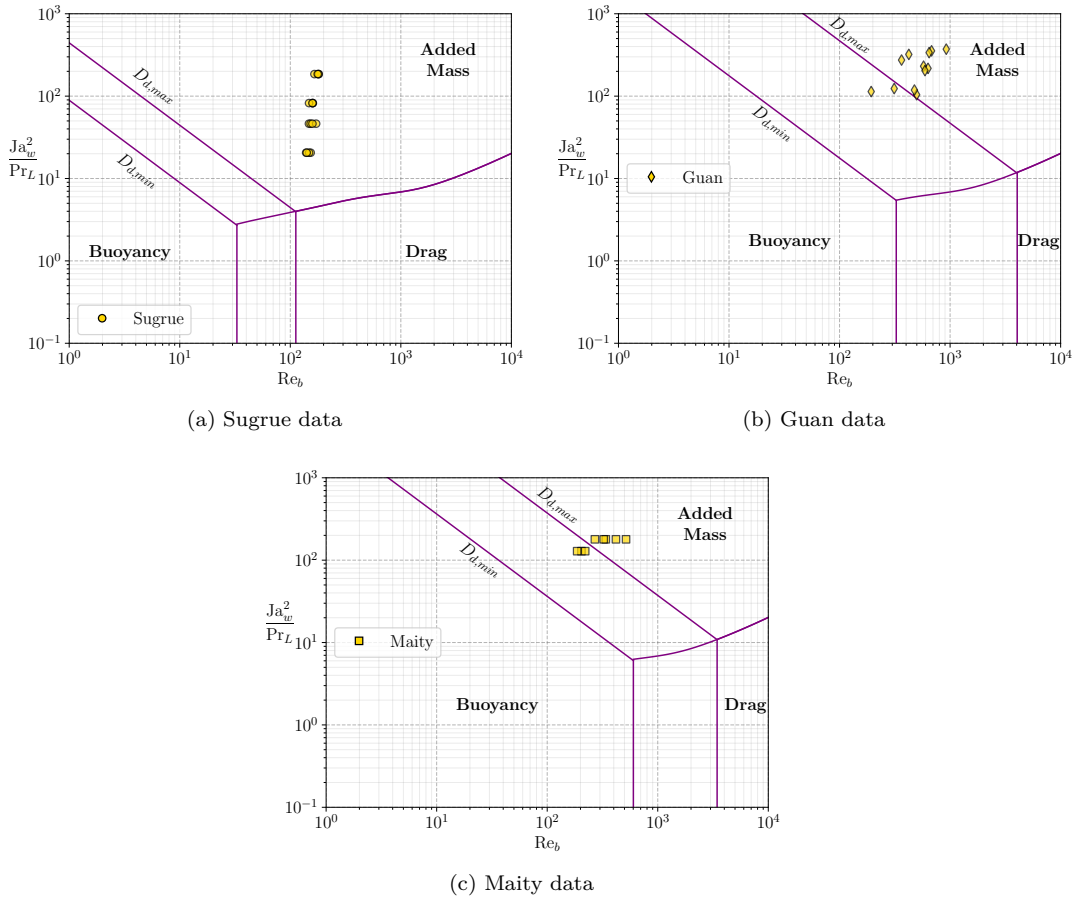


Figure 4.6: Dominance maps for each low pressure data sets.

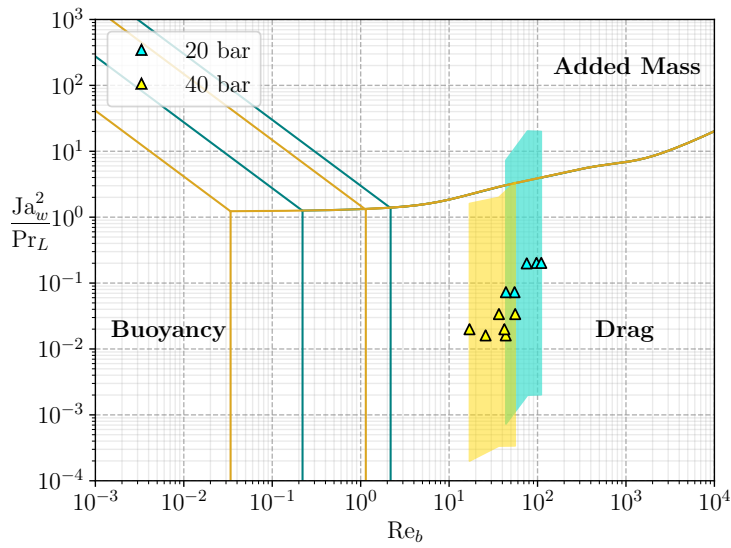
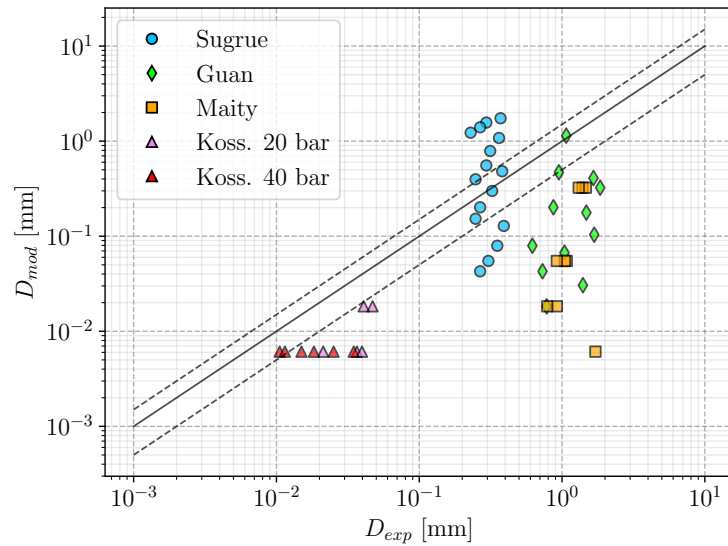
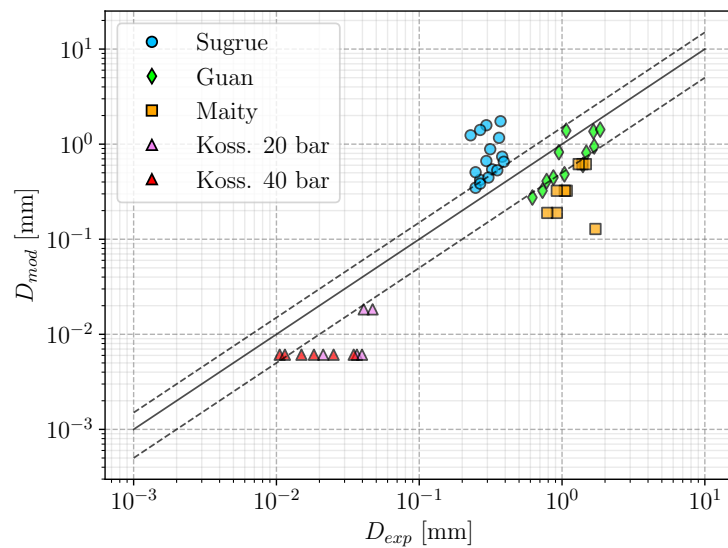


Figure 4.7: Dominance map for high pressure measurements from Kossolapov

Figure 4.8: D_d predictions using Eq. 4.34Figure 4.9: D_d predictions using Eq. 4.35

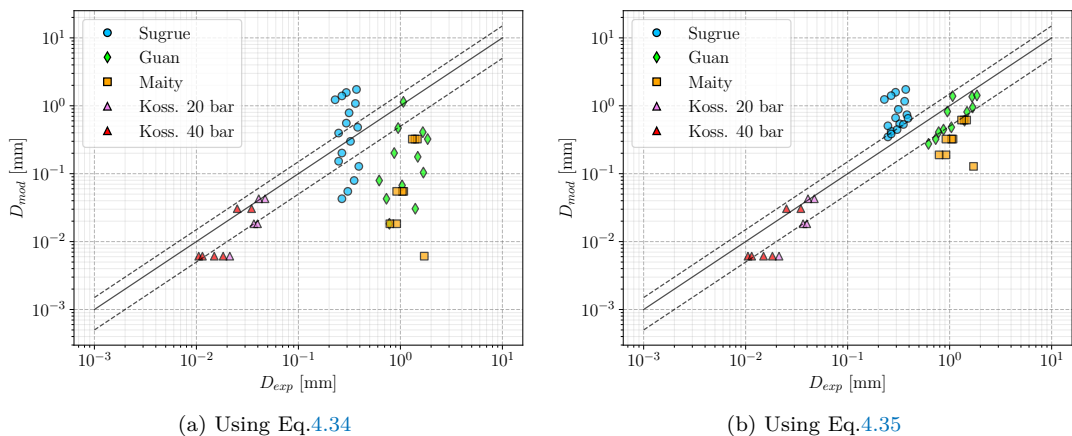


Figure 4.10: D_d predictions using $d\theta = 4^\circ$ for Kossolapov

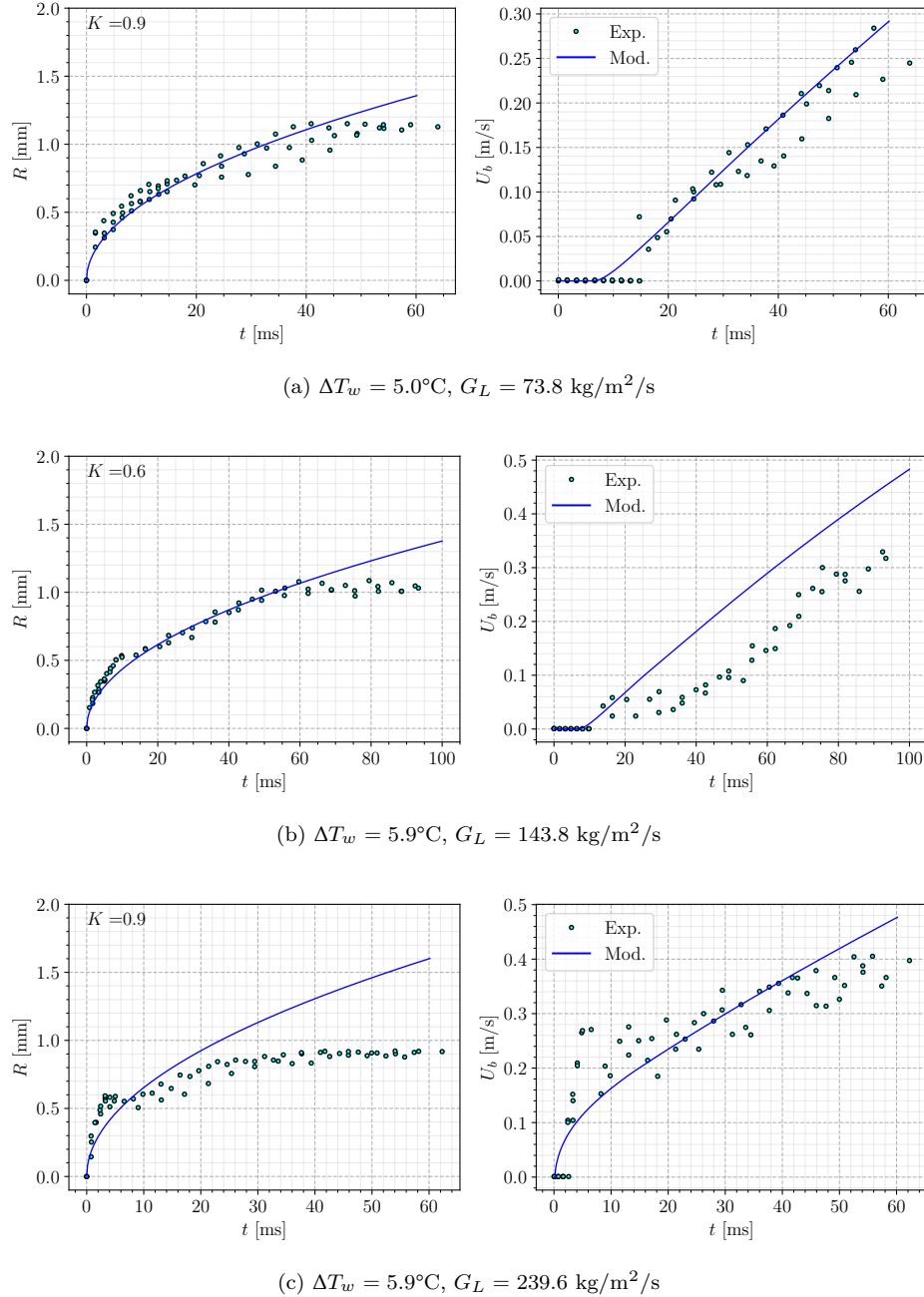


Figure 4.11: Bubble sliding velocity predictions on Maity cases

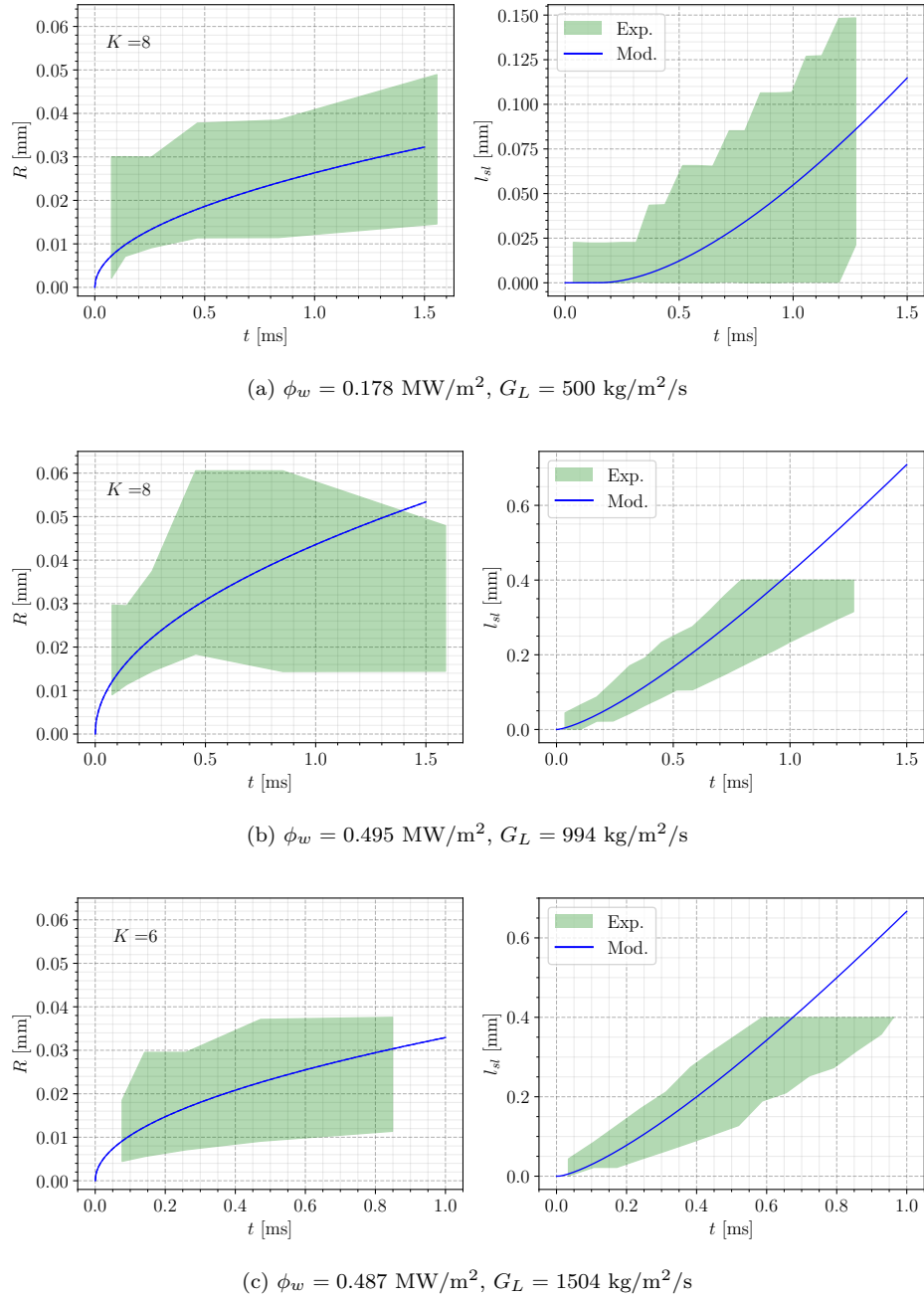


Figure 4.12: Bubble sliding length predictions on Kossolapov cases - $P = 20$ bar

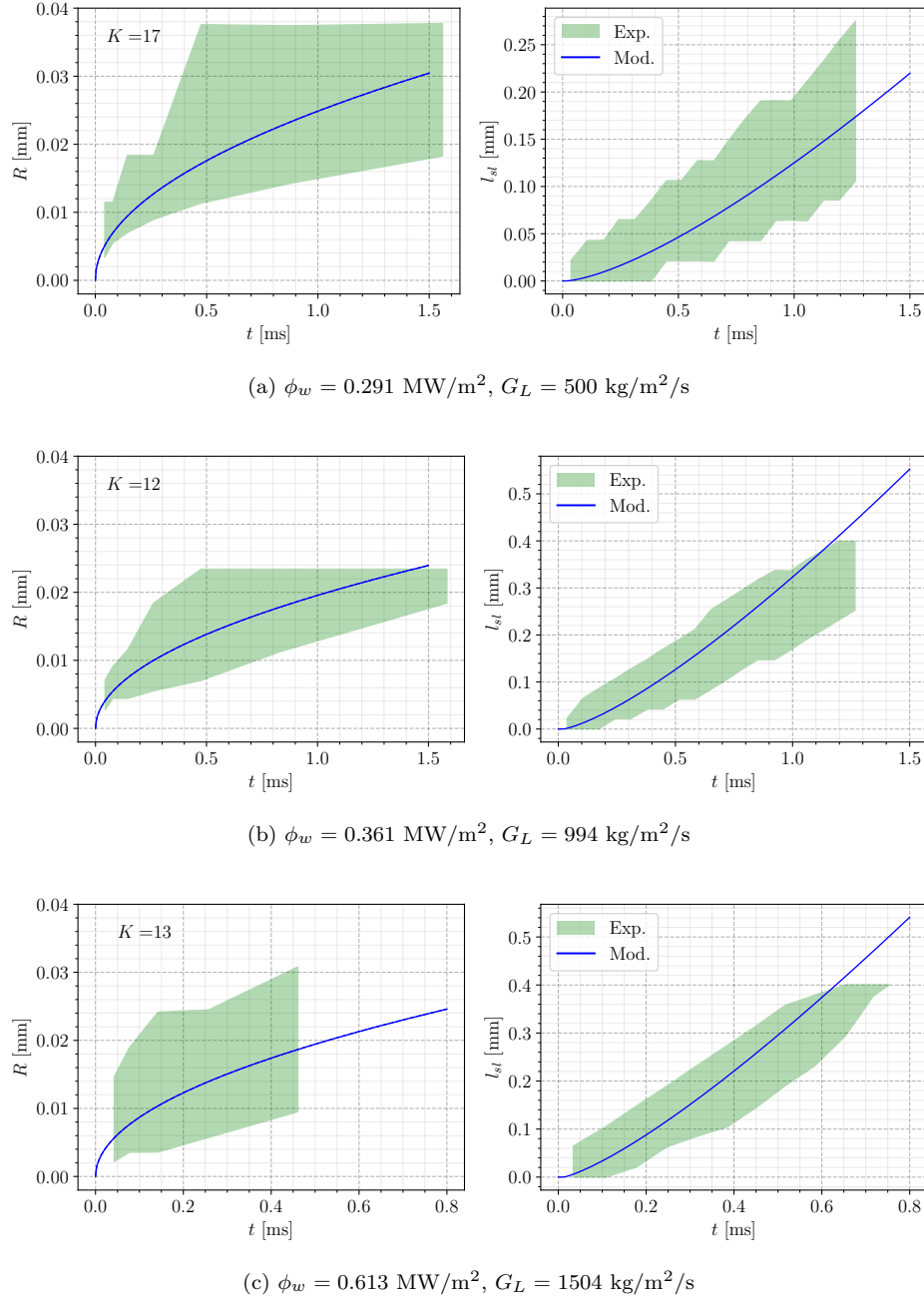


Figure 4.13: Bubble sliding length predictions on Kossolapov cases - $P = 40$ bar

When trying to understand the underlying physics behind departure and lift-off of growing bubbles on a wall, forces naturally come into the equations. Indeed, the critical diameters at which a bubble will leave its nucleation site to slide or lift-off from the surface are directly linked to the force balance applied to this very bubble.

Many authors have previously been tackling this issue to try to derive the whole force balance experienced by a bubble, starting with Klausner in 1993[CITE]. Since then, mechanistic approaches have been thoroughly studied to overcome empirical, correlation-based estimations of bubble departure and lift-off diameters[CITE]. The underlying idea is that if one manages to precisely compute the force balance applied to a bubble, it would lead to a high-fidelity representation of the bubble dynamics to evaluate its departure diameter D_d , sliding length l_{sl} , sliding velocity U_b and lift-off diameter D_{lo} .

However, the variety of hydrodynamics phenomena experienced by a boiling bubble in a flow makes the derivation of its force balance a very complicated task, in not impossible. This can only be achieved under many assumptions regarding bubble shape, external flow, etc. Moreover, the triggering of departure and lift-off can be associated to critical values of the force balance since many authors consider that the bubble starts moving when the balance is broken in one direction[CITE]. It is actually very delicate since it implies detecting a very small change in the whole force balance ($\sim nN$) resulting from the sum of forces of much greater magnitude ($\sim \mu N$)[CITE].

Nevertheless, studying the force balance can still provide interesting insights on bubble dynamics, particularly when comparing the impact of different forces depending on the operating conditions. That is why this chapter is dedicated to an analysis of the boiling bubble dynamics to try to understand a bit further the bubble behavior regarding the departure and sliding phenomenon in vertical flow boiling.

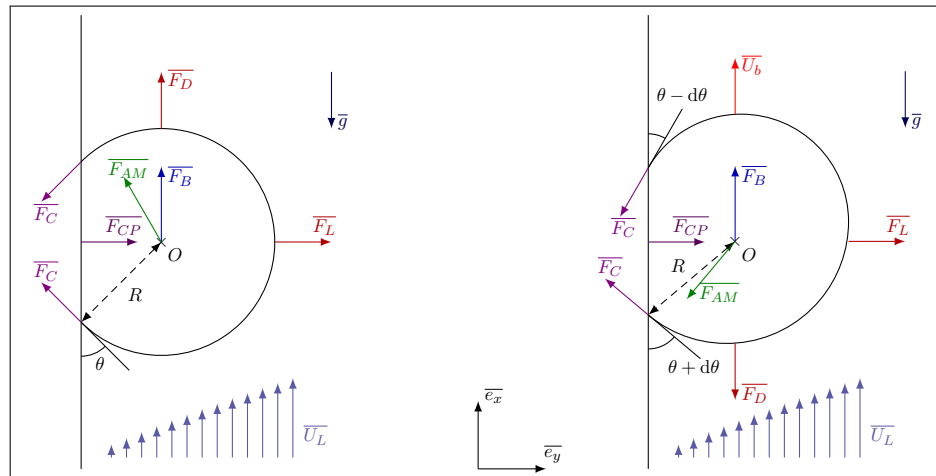


Figure 4.14: Bubble force balance in vertical flow boiling

4.5 ESTABLISHMENT OF THE FORCE BALANCE FOR A BUBBLE ON A VERTICAL WALL

In this section, we wish to detail expressions of the different forces experienced by the bubble and to compare their magnitude in order to assess which will be predominant in the departure and lift-off process.

4.5.1 Bubble shape : Geometrical definitions

In order to clearly express each of the considered forces, assumptions regarding the shape of the bubble nucleating at the wall are needed.

Here, we assume that the bubbles will mostly have the shape of a truncated sphere with respect to the contact angle θ_s (Fig. 4.15), being a thermophysical property of the fluid and the wall. This assumption can thoroughly be discussed since many experimental measurements and visualizations have shown that in the case of low pressure boiling, bubbles tend to be strongly deformed depending on the flow conditions (MAITY, ESTRADA-PÉREZ *et al.*, etc.) thus casting doubts on spherical or quasi-spherical hypotheses.

On the other hand, experiments conducted by KOSSOLAPOV found that in vertical flow boiling, increasing pressure leads to smaller and less deformable bubbles. Thus, supposing a truncated spherical shape could be relevant to model nucleating bubbles on a heater surface. Moreover, working on highly deformed bubbles would undoubtedly imply complicated calculations and extra parameters to account for.

KOSSOLAPOV's measurements also concluded that bubbles' inclination due to the flow nearly disappears at high pressures. However, since bubble tilt plays a great role in the surface tension force, we consider an angle tilt $d\theta$ compared to the static contact angle θ_s .

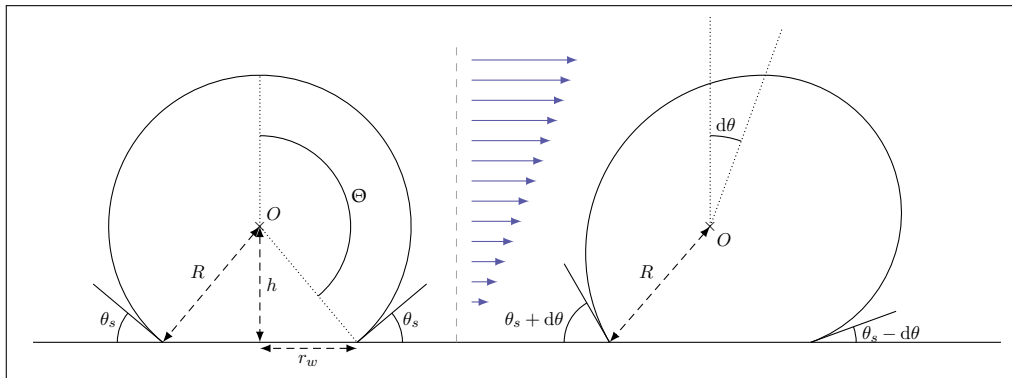


Figure 4.15: Sketch of the supposed bubble shape with (right) and without inclination (left).

The resulting bubble's volume V_b and projected area in the direction of the flow S_p can then be computed using the spherical coordinates system and defining the total angular portion covered by the bubble as $\Theta = \pi - \theta_s$, the bubble foot radius $r_w = R \sin(\theta_s)$ and the distance between the center of the bubble and the surface $h = R(1 + \cos(\theta_s))$, we have :

$$V_b = \underbrace{\int_{r=0}^R \int_{\theta=0}^{\Theta} \int_{\varphi=0}^{2\pi} r^2 \sin(\theta) dr d\theta d\varphi}_{\text{Spherical volume}} + \underbrace{\frac{1}{3}\pi r_w^2 h}_{\text{Conic volume}} = \frac{4}{3}\pi R^3 \left[\frac{1}{4}(2 - \cos(\theta_s))(1 + \cos(\theta_s))^2 \right] \quad (4.38)$$

$$S_p = \underbrace{\int_{r=0}^R \int_{\theta=-\Theta}^{\Theta} r dr d\theta}_{\text{Circular area}} + \underbrace{\frac{r_w h}{2\pi}}_{\text{Triangular area}} = \pi R^2 \left[1 - \frac{\theta_s}{\pi} + \frac{\sin(2\theta_s)}{2\pi} \right] \quad (4.39)$$

Thus, we can define shape factors that represent the ratio between the volume and projected areas of the truncated sphere compared to a complete sphere :

$$f_V(\theta_s) = \frac{V_{ts}}{V_s} = \frac{1}{4} (2 - \cos(\theta_s)) (1 + \cos(\theta_s))^2 \quad (4.40)$$

$$f_{S_p}(\theta_s) = \frac{S_{p,ts}}{S_{p,s}} = 1 - \frac{\theta_s}{\pi} + \frac{\sin(2\theta_s)}{2\pi} \quad (4.41)$$

Subscripts s and ts respectively denoting spherical and truncated spherical shapes.

Using those assumptions, we can thus express the volume of vapor generated for a single bubble up to its lift-off diameter $D_{lo} = 2R_{lo}$ (Eq. 4.42) :

$$V_b = \frac{4}{3}\pi R_{lo}^3 f_V(\theta_s) = \frac{\pi D_{lo}^3}{6} f_V(\theta_s) \quad (4.42)$$

As described in Section 4.5.1, we consider a bubble with a potential inclination $d\alpha$ from the static contact angle θ_s . Thus, the downstream contact angle is $\theta_d = \theta_s - d\theta$ and the upstream contact angle is $\theta_u = \theta_s + d\theta$ (Figure 4.15).

To estimate the bubble foot radius r_w of such a bubble, we can express it as the average between the two foot diameters for the advancing and receding contact angles :

$$r_w = \frac{1}{2} (\sin(\theta_d) R + \sin(\theta_u) R) = R \sin(\theta_s) \cos(d\theta) \quad (4.43)$$

In the following subsections, the vectors \bar{e}_{\parallel} and \bar{e}_{\perp} respectively represent the colinear and orthogonal vector to the wall surface.

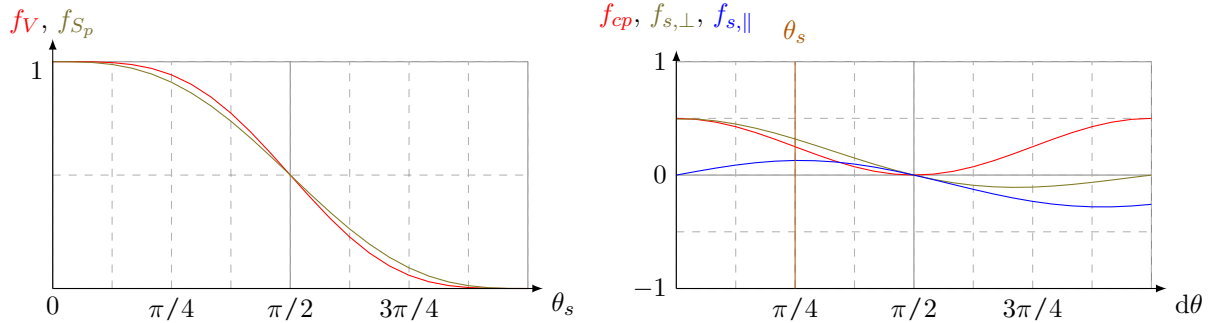


Figure 4.16: Representation of the shape functions

4.5.2 Buoyancy force

The well-known buoyancy force, also called Archimedes force, is computed by integration of the hydrostatic pressure exerted by the liquid over the bubble's surface and results in the difference between the gravity forces experienced by the vapour bubble and the equivalent liquid volume. The expression of this force \bar{F}_B is aligned with the gravity vector $\bar{g} = -g\bar{e}_x$.

$$\bar{F}_B = V_b (\rho_V - \rho_L) \bar{g} = \frac{4}{3}\pi R^3 f_V(\theta_s) (\rho_L - \rho_V) g \bar{e}_x \quad (4.44)$$

4.5.3 Contact Pressure force

The contact pressure force arises due to the pressure difference between the center of the bubble and the surrounding liquid. This pressure jump can be computed using LAPLACE's expression $\Delta P = 2\sigma/R_c$ where R_c is the curvature radius of the bubble's interface, being equal to R in the case of a spherical bubble. This pressure difference is then applied over the bubble foot area and results in a repelling force from the bubble's point of view, giving the resulting expression of $\overline{F_{CP}}$.

$$\overline{F_{CP}} = \frac{2\sigma}{R_c} \frac{\pi d_w^2}{4} \overline{e_y} \approx 2\sigma\pi R \underbrace{\sin^2(\theta) \cos^2(d\theta)}_{f_{CP}} \overline{e_\perp} = 2\pi R\sigma f_{CP}(\theta, d\theta) \overline{e_x} \quad (4.45)$$

(4.46)

4.5.4 Capillary force

The capillary or surface tension force results from the integration of the effort exerted over the triple contact line between the vapor inside the bubble, the surrounding liquid and the wall. This force has been derived by KLAUSNER[CITE] for a inclined bubble, yielding for each direction regarding the wall :

$$\begin{aligned} \overline{F_C} &= -1.25d_w\sigma \frac{\pi(\theta_u - \theta_d)}{\pi^2 - (\theta_u - \theta_d)^2} (\sin(\theta_u) + \sin(\theta_d)) \overline{e_x} - d_w\sigma \frac{\pi}{\theta_u - \theta_d} (\cos(\alpha_d) - \cos(\alpha_u)) \overline{e_y} \\ &\quad (4.47) \end{aligned}$$

$$\begin{aligned} &\approx -\pi R\sigma \underbrace{\left[1.25 \frac{2d\theta}{(\frac{\pi}{2})^2 - d\theta^2} \sin(\theta_s)^2 \cos(d\theta)^2 \right]}_{f_{C,x}} \overline{e_x} - \pi R\sigma \underbrace{\left[2 \sin(\theta_s)^2 \frac{\sin(2d\theta)}{2d\theta} \right]}_{f_{C,y}} \overline{e_y} \\ &\quad (4.48) \end{aligned}$$

$$= -\pi R\sigma f_{C,x}(\theta_s, d\theta) \overline{e_x} - \pi R\sigma f_{C,y}(\theta_s, d\theta) \overline{e_y} \quad (4.49)$$

4.5.5 Added Mass force of a growing bubble

Added mass effects are experienced by the bubble :

- when its boundary is moving during its growth
- when accelerating while sliding on the wall
- when the surrounding liquid is accelerating

We consider a spherical cap shaped bubble standing on a plane wall and facing an uniform liquid velocity U . In this situation, Van Der Geld derived the potential flow around the bubble and expressed the liquid kinetic energy, obtaining :

$$T_L = \rho_L V_b \left(\frac{1}{2} \alpha \dot{y}^2 + \frac{1}{2} \text{tr}(\beta) \dot{R}^2 + \frac{1}{2} \psi \dot{R} \dot{y} + \frac{1}{2} \alpha_2 U^2 \right) \quad (4.50)$$

where α , $\text{tr}(\beta)$, ψ and α_2 are polynomials of $\lambda = \frac{R}{2h}$. We also have x and $y = h$ denoting the coordinates of the geometrical center of the bubble.

Therefore, we can write those coefficients in the following form :

$$\alpha = \sum_{k=0}^n \alpha_k \frac{R^k}{2^k y^k} \quad (4.51)$$

If we suppose that the generalized coordinates and velocities x , \dot{x} , y , \dot{y} , R , and \dot{R} , we can use the expression of the kinetic energy of the fluid to apply Lagrange's equations to derive the added mass forces on the bubble in both direction parallel and normal to the wall :

$$F_{AM,x} = -\frac{\partial}{\partial t} \left(\frac{\partial T_L}{\partial \dot{x}} \right) + \frac{\partial T_L}{\partial x} \quad (4.52)$$

$$F_{AM,y} = -\frac{\partial}{\partial t} \left(\frac{\partial T_L}{\partial \dot{y}} \right) + \frac{\partial T_L}{\partial y} \quad (4.53)$$

In the case of the sliding bubble, we replace the uniform liquid velocity U by the relative velocity experienced by the bubble $U_{rel} = U_{liq} - \dot{x}$ where U_{liq} is the uniform surrounding liquid velocity and \dot{x} the velocity of the center of the bubble, which is the sliding velocity of the bubble. Yielding :

$$T_L = \frac{\rho_L V_b}{2} \left(\alpha \dot{y}^2 + \text{tr}(\beta) \dot{R}^2 + \psi \dot{R} \dot{y} + \alpha_2 (U_{liq} - \dot{x})^2 \right) \quad (4.54)$$

ADDED MASS IN x DIRECTION Parallel to the wall, since λ depends on y and R , it is independent of \dot{x} , yielding zero-derivatives for the added mass coefficients. We can write :

$$\frac{\partial T_L}{\partial \dot{x}} = \frac{\rho_L V_b}{2} \alpha_2 \frac{\partial ((U_{liq} - \dot{x})^2)}{\partial \dot{x}} \quad (4.55)$$

$$= \rho_L V_b \alpha_2 (\dot{x} - U_{liq}) \quad (4.56)$$

$$(4.57)$$

As for the time derivatives, we have :

$$\frac{\partial V_b}{\partial t} = \frac{\partial \frac{4}{3}\pi R^3}{\partial t} = 4\pi R^2 \dot{R} \quad (4.58)$$

$$\frac{\partial \lambda}{\partial t} = \frac{\dot{R} 2y - R 2\dot{y}}{4y^2} = \lambda \left(\frac{\dot{R}}{R} - \frac{\dot{y}}{y} \right) = \lambda \left(\frac{\dot{R}}{R} - 2\lambda \frac{\dot{y}}{R} \right) = \frac{\lambda}{R} (\dot{R} - 2\lambda \dot{y}) \quad (4.59)$$

$$\frac{\partial \alpha}{\partial t} = \sum_{k=0}^n \alpha_k \frac{\partial \lambda^k}{\partial t} = \sum_{k=0}^n \alpha_k k \lambda^{k-1} \frac{\partial \lambda}{\partial t} = \left(\frac{\dot{R}}{R} - \frac{\dot{y}}{y} \right) \underbrace{\sum_{k=0}^n \alpha_k k \lambda^k}_{\tilde{\alpha}} = \frac{1}{R} (\dot{R} - 2\lambda \dot{y}) \tilde{\alpha} \quad (4.60)$$

Yielding :

$$\frac{\partial}{\partial t} \left(\frac{\partial T_L}{\partial \dot{x}} \right) = \rho_L \left[4\pi R^2 \dot{R} \alpha_2 (\dot{x} - U_{liq}) + \frac{4}{3} \pi R^3 \left(\frac{\dot{R}}{R} - \frac{\dot{y}}{y} \right) \tilde{\alpha}_2 (\dot{x} - U_{liq}) + \frac{4}{3} \pi R^3 \alpha_2 \ddot{x} \right] \quad (4.61)$$

$$= 4\pi R^2 \rho_L \left[\alpha_2 \dot{R} (\dot{x} - U_{liq}) + \frac{\tilde{\alpha}_2}{3} (\dot{R} - 2\lambda \dot{y}) (\dot{x} - U_{liq}) + \frac{R}{3} \alpha_2 \ddot{x} \right] \quad (4.62)$$

$$= 4\pi R^2 \rho_L \left[\left(\alpha_2 + \frac{\tilde{\alpha}_2}{3} \right) \dot{R} (\dot{x} - U_{liq}) - \frac{2}{3} \lambda \tilde{\alpha}_2 \dot{y} (\dot{x} - U_{liq}) + \frac{R}{3} \alpha_2 \ddot{x} \right] \quad (4.63)$$

We also have, with the independence of the variables :

$$\frac{\partial T_L}{\partial x} = 0 \quad (4.64)$$

Finally yielding,

$$F_{AM,x} = 4\pi R^2 \rho_L \left[\left(\alpha_2 + \frac{\tilde{\alpha}_2}{3} \right) \dot{R} U_{rel} - \frac{2}{3} \lambda \tilde{\alpha}_2 \dot{y} U_{rel} - \frac{R}{3} \alpha_2 \ddot{x} \right] \quad (4.65)$$

We can immediately observe that the added mass related to the bubble growth will promote detachment when the bubble is still attached to its nucleation site ($\dot{x} = 0$). This contradicts the often-used approach using solely the Rayleigh-Plesset equation projected in both direction using the inclination angle of the bubble.

The other part of this added-mass force is naturally linked to the acceleration of the bubble and the mass of displaced liquid.

ADDED MASS IN y DIRECTION Following the same approach normal to the wall, we obtain :

$$\frac{\partial T_L}{\partial \dot{y}} = \frac{1}{2} \rho_L \frac{4}{3} \pi R^3 (\alpha_2 \dot{y} + \psi \dot{R}) = \rho_L \frac{4}{3} \pi R^3 \left(\alpha \dot{y} + \frac{\psi}{2} \dot{R} \right) \quad (4.66)$$

$$\frac{\partial}{\partial t} \left(\frac{\partial T_L}{\partial \dot{y}} \right) = \rho_L 4\pi R^2 \dot{R} \left(\alpha \dot{y} + \frac{1}{2} \psi \dot{R} \right) + \rho_L \frac{4}{3} \pi R^3 \left(\frac{1}{R} (\dot{R} - 2\lambda \dot{y}) \tilde{\alpha} \dot{y} + \alpha \ddot{y} + \frac{1}{2} \tilde{\psi} \frac{1}{R} (\dot{R} - 2\lambda \dot{y}) \dot{R} + \frac{1}{2} \psi \ddot{R} \right) \quad (4.67)$$

$$= \rho_L 4\pi R^2 \left[\frac{\alpha}{3} R \ddot{y} + \frac{\psi}{6} R \ddot{R} + \left(\frac{\psi}{2} + \frac{\tilde{\psi}}{6} \right) \dot{R}^2 - \frac{2}{3} \lambda \tilde{\alpha} \dot{y}^2 + \left(\alpha + \frac{\tilde{\alpha}}{3} - \frac{\tilde{\psi}}{3} \right) \dot{R} \dot{y} \right] \quad (4.68)$$

$$\frac{\partial T_L}{\partial y} = \rho_L \frac{4}{3} \pi R^3 \left(\frac{1}{2} \frac{\partial \alpha}{\partial y} \dot{y}^2 + \frac{1}{2} \frac{\partial \text{tr}(\beta)}{\partial y} \dot{R}^2 + \frac{1}{2} \frac{\partial \psi}{\partial y} \dot{R} \dot{y} + \frac{1}{2} \frac{\partial \alpha_2}{\partial y} (U_{liq} - \dot{x})^2 \right) \quad (4.69)$$

Where we can write :

$$\frac{\partial \alpha}{\partial y} = \sum_{k=0}^n \alpha_k \frac{\partial \lambda^k}{\partial y} = \sum_{k=0}^n \alpha_k \frac{R^k}{2^k} \frac{\partial}{\partial y} \left(\frac{1}{y^k} \right) = \sum_{k=0}^n \alpha_k \frac{R^k}{2^k} (-k) \frac{1}{y^{k+1}} = \frac{1}{y} \sum_{k=0}^n (-k) \alpha_k \lambda^k = -\frac{1}{y} \tilde{\alpha} \quad (4.70)$$

Giving :

$$\frac{\partial T_L}{\partial y} = \rho_L 4\pi R^2 \frac{R}{6y} \left[-\tilde{\alpha}\dot{y}^2 - \text{tr}(\tilde{\beta})\dot{R}^2 - \tilde{\psi}\dot{R}\dot{y} - \tilde{\alpha}_2 U_{rel}^2 \right] \quad (4.71)$$

$$= -\rho_L 4\pi R^2 \frac{\lambda}{3} \left[\tilde{\alpha}\dot{y}^2 + \text{tr}(\tilde{\beta})\dot{R}^2 + \tilde{\psi}\dot{R}\dot{y} + \tilde{\alpha}_2 U_{rel}^2 \right] \quad (4.72)$$

Which finally yields :

$$F_{AM,y} = -\rho_L 4\pi R^2 \left[\frac{\alpha}{3} R\ddot{y} + \frac{\psi}{6} R\ddot{R} + \left(\frac{\psi}{2} + \frac{\tilde{\psi}}{6} \right) \dot{R}^2 - \frac{2}{3} \lambda \tilde{\alpha} \dot{y}^2 + \left(\alpha + \frac{\tilde{\alpha}}{3} - \frac{\tilde{\psi}}{3} \right) \dot{R}\dot{y} \right] \\ - \rho_L 4\pi R^2 \frac{\lambda}{3} \left[\tilde{\alpha}\dot{y}^2 + \text{tr}(\tilde{\beta})\dot{R}^2 + \tilde{\psi}\dot{R}\dot{y} + \tilde{\alpha}_2 U_{rel}^2 \right] \quad (4.73)$$

$$= \rho_L 4\pi R^2 \left[\frac{\lambda}{3} \tilde{\alpha} \dot{y}^2 + \left(-\frac{\lambda}{3} \text{tr}(\tilde{\beta}) - \frac{\psi}{2} - \frac{\tilde{\psi}}{6} \right) \dot{R}^2 + \left(-\alpha - \frac{\tilde{\alpha}}{3} + \frac{1-\lambda}{3} \tilde{\psi} \right) \dot{R}\dot{y} - \frac{\alpha}{3} R\ddot{y} - \frac{\psi}{6} R\ddot{R} - \frac{\lambda}{3} \tilde{\alpha}_2 U_{rel}^2 \right] \quad (4.74)$$

Where :

$$\alpha = 111.62137 - 844.131315\lambda + 2678.058461\lambda^2 - 4534.349913\lambda^3 \\ + 4311.889654\lambda^4 - 2180.345705\lambda^5 + 457.591961\lambda^6 \quad (4.75)$$

$$\psi = -220.824854 + 1639.114567\lambda - 5130.691427\lambda^2 + 8625.857798\lambda^3 \\ - 8169.91248\lambda^4 + 4121.492877\lambda^5 - 863.784836\lambda^6 \quad (4.76)$$

$$\text{tr}(\beta) = 104.601303 - 736.214699\lambda + 2293.784611\lambda^2 - 3857.878559\lambda^3 \\ + 3659.95521\lambda^4 - 1849.854303\lambda^5 + 388.412909\lambda^6 \quad (4.77)$$

$$\alpha_2 = 0.359528 + 1.341274\lambda - 1.973813\lambda^2 + 0.796613\lambda^3 \quad (4.78)$$

If we define added mass coefficients C_{AM} as :

$$F_{AM,x} = \pi R^2 \rho_L (C_{AM,x1} \dot{R} U_{rel} + C_{AM,x2} \dot{y} U_{rel} + C_{AM,x3} R \ddot{x}) \quad (4.79)$$

$$F_{AM,y} = \pi R^2 \rho_L (C_{AM,y1} \dot{y}^2 + C_{AM,y2} \dot{R}^2 + C_{AM,y3} \dot{R}\dot{y} + C_{AM,y4} R\ddot{y} + C_{AM,y5} R\ddot{R} + C_{AM,y6} U_{rel}^2) \quad (4.80)$$

We obtain :

$$C_{AM,x1} = 6.372904\lambda^3 - 13.1587533\lambda^2 + 7.15346133\lambda + 1.438112 \quad (4.81)$$

$$C_{AM,x2} = -6.372904\lambda^4 + 10.527002667\lambda^3 - 3.576730667\lambda^2 \quad (4.82)$$

$$C_{AM,x3} = -1.062150667\lambda^3 + 2.631750667\lambda^2 - 1.78836533\lambda - 0.479370667 \quad (4.83)$$

$$\begin{aligned} C_{AM,y1} = & 3660.735688\lambda^7 - 14535.638033\lambda^6 + 22996.74482133\lambda^5 - 18137.399652\lambda^4 + 7141.48922933\lambda^3 \\ & - 1125.50842\lambda^2 \end{aligned} \quad (4.84)$$

$$\begin{aligned} C_{AM,y2} = & -3107.303272\lambda^7 + 17515.071036\lambda^6 - 41501.056736\lambda^5 + 53557.772476\lambda^4 - 40620.190154667\lambda^3 \\ & + 18083.92435533\lambda^2 - 4370.972178667\lambda + 441.649708 \end{aligned} \quad (4.85)$$

$$\begin{aligned} C_{AM,y3} = & 6910.278688\lambda^7 - 39878.0014\lambda^6 + 94306.5065933\lambda^5 - 118320.60118933\lambda^4 + 84460.07430133\lambda^3 \\ & - 33721.052968\lambda^2 + 6687.51976933\lambda - 446.48548 \end{aligned} \quad (4.86)$$

$$\begin{aligned} C_{AM,y4} = & -610.122614667\lambda^6 + 2907.12760667\lambda^5 - 5749.18620533\lambda^4 + 6045.799884\lambda^3 \\ & - 3570.744614667\lambda^2 + 1125.50842\lambda - 148.8284933 \end{aligned} \quad (4.87)$$

$$\begin{aligned} C_{AM,y5} = & 575.85655733\lambda^6 - 2747.661918\lambda^5 + 5446.60832\lambda^4 - 5750.57186533\lambda^3 \\ & + 3420.46095133\lambda^2 - 1092.743044667\lambda + 147.21656933 \end{aligned} \quad (4.88)$$

$$C_{AM,y6} = -3.186452\lambda^4 + 5.26350133\lambda^3 - 1.78836533\lambda^2 \quad (4.89)$$

$$(4.90)$$

In the case of the full or truncated sphere on a wall, we can write $y = R\cos(\theta)$ and $\dot{y} = \dot{R}\cos(\theta)$ if we suppose a quasi-constant contact angle during bubble lifetime. Moreover, $\lambda = 1/2\cos(\theta)$.

The added-mass forces then become :

$$F_{AM,x} = \rho_L \pi R^2 [(C_{AM,x1} + C_{AM,x2}\cos(\theta)) \dot{R}U_{rel} + C_{AM,x3}R\ddot{x}] \quad (4.91)$$

$$F_{AM,y} = \rho_L \pi R^2 \left[\left(C_{AM,y1}\cos(\theta)^2 + C_{AM,y2} + C_{AM,y3}\cos(\theta) \right) \dot{R}^2 + (C_{AM,y4}\cos(\theta) + C_{AM,y5}) R\ddot{R} + C_{AM,y6}U_{rel}^2 \right] \quad (4.92)$$

Finally, if we consider the full sphere case : $\theta = 0$ and $\lambda = 0.5$, we can estimate the numerical values of the sphere added mass coefficients $C_{AM,S}$:

$$F_{AM,x} = \rho_L \pi R^2 [C_{AM,Sx1}\dot{R}U_{rel} + C_{AM,Sx2}R\ddot{x}] \quad (4.93)$$

$$F_{AM,y} = \rho_L \pi R^2 [C_{AM,Sy1}\dot{R}^2 + C_{AM,Sy2}R\ddot{R} + C_{AM,Sy3}U_{rel}^2] \quad (4.94)$$

where $C_{AM,Sx1} \approx 2.5451535$; $C_{AM,Sx2} \approx -0.8483845$

$C_{AM,Sy1} \approx 4.774859833$; $C_{AM,Sy2} \approx -0.359872041667$ and $C_{AM,Sy3} \approx 0.0116930833$

4.5.6 Added Mass from Duhar et al.

$$\overline{F_{AM}} = -\rho_L \frac{d}{dt} \left[V_b \frac{1}{2} \left(1 + \frac{3}{16} \left(\frac{R}{y} \right)^3 \right) (U_{b,x} - U_L) \overline{e_x} + V_b \frac{1}{2} \left(1 + \frac{3}{8} \left(\frac{R}{y} \right)^3 \right) U_{b,y} \overline{e_y} \right] \quad (4.95)$$

$$+ \frac{3}{32} \rho_L \frac{d^2}{dt^2} (RV_b) \left(\frac{R}{y} \right)^2 \overline{e_y} + \frac{\pi R^2}{2} \left(\frac{R}{y} \right)^4 \left[\frac{3}{8} U_{rel}^2 + \frac{3}{4} U_{b,y}^2 \right] \overline{e_y} \quad (4.96)$$

Yielding :

$$\overline{F_{AM}} \cdot \overline{e_x} = \frac{\rho_L V_b}{2} \left[3 \left(1 + \frac{3}{16} \left(\frac{R}{y} \right)^3 \right) \frac{\dot{R}}{R} U_{rel} + \frac{9}{16} \left(\frac{R}{y} \right)^3 \left(\frac{\dot{R}}{R} - \frac{\dot{y}}{y} \right) U_{rel} - \left(1 + \frac{3}{16} \left(\frac{R}{y} \right)^3 \right) \frac{\partial U_{b,x}}{\partial t} \right] \quad (4.97)$$

$$\overline{F_{AM}} \cdot \overline{e_y} = \frac{-\rho_L V_b}{2} \left[3 \left(1 + \frac{3}{8} \left(\frac{R}{y} \right)^3 \right) \frac{\dot{R}}{R} U_{b,y} + \frac{3}{8} \left(\frac{R}{y} \right)^3 \left(\frac{\dot{R}}{R} - \frac{\dot{y}}{y} \right) U_{b,y} + \left(1 + \frac{3}{8} \left(\frac{R}{y} \right)^3 \right) \frac{\partial U_{b,y}}{\partial t} \right] \quad (4.98)$$

$$\frac{\rho_L V_b}{2} \left[\frac{3}{4} \left(\frac{R}{y} \right)^2 \left(\ddot{R} + 3 \frac{\dot{R}^2}{R} \right) \right] + \frac{\rho_L V_b}{2} \left[\frac{3}{4} \left(\frac{R}{y} \right)^4 \left(\frac{3}{8} \frac{U_{rel}^2}{R} + \frac{3}{4} \frac{U_{b,y}}{R} \right) \right] \quad (4.99)$$

4.5.7 Lift and drag forces

The lift force and the drag force represent the two components of the global hydrodynamic effort exerted by the surrounding flow over a bubble. The lift force corresponds to the force directed orthogonally to the flow direction while the drag is the colinear one.

Those forces are usually expressed using both the projected area of the bubble facing the flow and the relative velocity along with a lift coefficient C_L and a drag coefficient C_D respectively.

$$\overline{F_D} = \frac{1}{2} C_D S_p \rho_l U_{rel}^2 \overline{e_{||}} \quad (4.100)$$

$$= \frac{1}{2} C_D \pi R^2 f_{S_p}(\alpha) \rho_l U_{rel}^2 \overline{e_{||}} \quad (4.101)$$

$$\overline{F_L} = \frac{1}{2} C_L S_p \rho_l U_{rel}^2 \overline{e_{\perp}} \quad (4.102)$$

$$= \frac{1}{2} C_L \pi R^2 f_{S_p}(\alpha) \rho_l U_{rel}^2 \overline{e_{\perp}} \quad (4.103)$$

In those two expressions, the main parameter remains C_D and C_L which modeling can be developed depending on the flow characteristics (uniform, shear, wall influence, etc.). For instance, one of the most recent and complete expression of those coefficients have been derived from DNS conducted by Shi *et al.* which takes into account the distance to the wall and the shear rate simultaneously.

4.5.7.1 Drag and lift coefficient from Shi *et al.*

In this section, we detail the expression of the drag and lift coefficient derived by Shi *et al.* from multiple DNS simulations.

The following notations are proper to this sub-section of the document. Variables used by Shi *et al.* to describe drag and lift are detailed on Table 4.4

The drag and lift coefficient are computed from their DNS results by integrating the hydrodynamic effort over the bubble's surface. The axial and radial component respectively yielding the drag and lift coefficient when divided by $\pi d^2 \rho_l U_{rel}^2 / 8$.

Name	Definition	Unit
d	Bubble diameter	m
γ	Flow shear rate	s ⁻¹
\tilde{L}	Distance to the wall	m
\tilde{L}_u	$\nu_l / U_{rel} $	m
\tilde{L}_ω	$\sqrt{\nu_l / \omega}$	m
L_u	\tilde{L} / \tilde{L}_u	(-)
L_ω	$\tilde{L} / \tilde{L}_\omega$	(-)
L_R	$2\tilde{L}/d$	(-)
Re	$ U_{rel} d / \nu_l$	(-)
Sr	$\gamma d / U_{rel}$	(-)
ε	$\tilde{L}_u / \tilde{L}_\omega = \sqrt{ \text{Sr} / \text{Re}}$	(-)

Table 4.4: Variables used by Shi *et al.*

DRAG COEFFICIENT : The total drag coefficient is expressed as a correction ΔC_D^W of a uniform drag coefficient C_{D0}^U to account for shear and wall effects :

$$C_D^W = \Delta C_D^W C_{D0}^U + C_{D0}^U = C_{D0}^U \left(1 + \Delta C_D^W \right) \quad (4.104)$$

$$\text{with } C_{D0}^U (\text{Re} \gg 1) = \frac{48}{\text{Re}} \quad (\text{Kang and Leal, 1988}) \quad (4.105)$$

$$\Delta C_D^W (\text{Re}) \approx \Delta C_D^W [\text{Re} = O(1)] + c_{D\omega\infty} \Delta C_D^W (\text{Re} \gg 1) \quad (4.106)$$

$$\text{with } c_{D\omega\infty} = 1 - e^{-0.07\text{Re}} \quad (4.107)$$

$$\Delta C_D^W [\text{Re} = O(1)] \approx f'_D (L_u) b^2 (\text{Re}) \Delta C_D^{\text{W-in}} \quad (4.108)$$

$$f'_D (L_u) \approx \frac{1}{1 + 0.16L_u (L_u + 4)} \quad (4.109)$$

$$b (\text{Re}) = 1 + \tanh (0.012\text{Re}^{0.8}) + \tanh (0.07\text{Re}^{0.8}) \quad (4.110)$$

$$\Delta C_D^{\text{W-in}} (\text{Sr}, L_R) = \left(\frac{3}{8} L_R^{-1} + \frac{3}{64} L_R^{-4} \right) \left(1 - \frac{3}{8} L_R^{-1} - \frac{3}{64} L_R^{-4} \right)^{-1} - \frac{1}{16} \left(L_R^{-2} + \frac{3}{8} L_R^{-3} \right) \text{Sr} \quad (4.111)$$

They actually operate a blending between a high Reynolds and a low Reynolds expression, which have both been derived from their numerical results :

$$\Delta C_D^W (\text{Re} \gg 1) \approx \Delta C_{Du}^W (\text{Re} \gg 1) + \Delta C_{D\omega}^U (\text{Re} \gg 1) + \Delta C_{D\omega}^{W-U} (\text{Re} \gg 1) \quad (4.112)$$

$$\Delta C_{Du}^W (\text{Re} \gg 1) \approx 0.47 L_R^{-4} + 5.5 \times 10^{-3} L_R^{-6} \text{Re}^{3/4} \quad (4.113)$$

$$\Delta C_{D\omega}^U (\text{Re} \gg 1) \approx 2 \times 10^{-3} |\text{Sr}|^{1.9} \text{Re} \quad (4.114)$$

$$\Delta C_{D\omega}^{W-U} (\text{Re} \gg 1) \approx 0.05 L_R^{-7/2} \text{Sr} \text{Re}^{1/3} \quad (4.115)$$

LIFT COEFFICIENT : The total lift coefficient C_L^W is expressed as :

$$C_L^W(\text{Re}, \text{Sr}, L_R) = C_{Lu}^W(\text{Re}, \text{Sr}, L_R) + C_{L\omega}^W(\text{Re}, \text{Sr}, L_R) \quad (4.116)$$

which corresponds to the superposition of two contributions being the uniform flow and the shear rate, both in presence of the wall.

$$C_{Lu}^W(\text{Re}, \text{Sr}, L_R) \approx f_L f'_L b^2 (L_R/3)^g C_{Lu}^{\text{W-in}} + c_{T1} \left[C_{Lu}^W(\text{Re} \rightarrow \infty) + c_{T2} \text{Re}^{-1} L_R^{-4} \right] \quad (4.117)$$

$$f_L(L_\omega, \varepsilon) = e^{-0.22\varepsilon^{0.8} L_\omega^{2.5}} \quad (4.118)$$

$$f'_L(L_u) \approx \frac{1}{1 + 0.13L_u(L_u + 0.53)} \quad (4.119)$$

$$b(\text{Re}) = 1 + \tanh(0.012\text{Re}^{0.8}) + \tanh(0.07\text{Re}^{0.8}) \quad (4.120)$$

$$g = -2.0 \tanh(0.01\text{Re}) \quad (4.121)$$

$$C_{Lu}^{\text{W-in}} = \frac{1}{2} \left(1 + \frac{1}{8} L_R^{-1} - \frac{33}{64} L_R^{-2} \right) \quad (4.122)$$

$$c_{T1}(\text{Re}) = 1 - e^{-0.22\text{Re}^{0.6}} \quad (4.123)$$

$$C_{Lu}^W(\text{Re} \rightarrow \infty) \approx -\frac{3}{8} L_R^{-4} \left[1 + \frac{1}{8} L_R^{-3} + \frac{1}{6} L_R^{-5} \right] + O(L_R^{-10}) \quad (4.124)$$

$$c_{T2} = 15 \tanh(0.01\text{Re}) \quad (4.125)$$

$$C_{L\omega}^W(\text{Re}, \text{Sr}, L_R) \approx h'_L C_{L\omega}^U(\text{Re} \ll 1) + c_{T3}(\text{Re})(1 + I_{WS}) C_{L\omega}^U(\text{Re} \gg 1) \quad (4.126)$$

$$\text{with } c_{T3}(\text{Re}) = 1 - e^{-0.3\text{Re}} \quad (4.127)$$

$$h'_L(L_\omega, \varepsilon, L_R) = 1 - e^{-\frac{11}{96}\pi^2 \frac{L_\omega}{J_L(\varepsilon)} (1 + \frac{9}{8}L_R^{-1} - \frac{1271}{3520}L_R^{-2})} \quad (4.128)$$

$$J_L(\varepsilon) = J_L(\infty) (1 + 0.2\varepsilon^{-2})^{-3/2} \text{ with } J_L(\infty) = 2.254 \quad (4.129)$$

$$C_{L\omega}^U(\text{Re} \ll 1) = \frac{8}{\pi^2} \frac{\text{Sr}}{|Sr|} \varepsilon J_L(\varepsilon) \quad (4.130)$$

$$I_{WS} = a_G L_R^{-7/2} \left(1 + b_G \text{Re}^{-1/2} \right) \text{ with } a_G = 0.23 \text{ and } b_G = 13 \quad (4.131)$$

$$C_{L\omega}^U(\text{Re} \gg 1) = \frac{2}{3} \text{Sr} (1 - 0.07 |Sr|) \frac{1 + 16\text{Re}^{-1}}{1 + 29\text{Re}^{-1}} \quad (4.132)$$

4.5.8 Dominant Forces at Departure by Sliding

Once each forces has been described, we can write the whole force balance parallel to the wall for a bubble prior to the departure by sliding. Since we further need expressions for R and \dot{R} , we suppose $R(t) = K \text{Ja}_w \sqrt{\eta_l t}$ with $K \approx 2$ for the early stage of bubble growth as proposed and validated in different research works [Plessset1954, Klausner1993]. Before departure, we have $\overline{U_b} = \overline{0}$. The total force balance parallel to the wall then yields :

$$-\pi R \sigma f_{C,x}(\theta, d\theta) + V_b (\rho_L - \rho_V) g + \frac{1}{2} C_D \rho_L S_p U_L^2 + \rho_L V_0 C_{AM,x1} \frac{\dot{R}}{R} U_L = 0 \quad (4.133)$$

with $f_{C,x} = 2.5 \frac{d\theta}{(\pi/2)^2 - d\theta^2} \sin(\theta)^2 \cos(d\theta)^2 \rightarrow 0$ if $d\theta \rightarrow 0$; $V_b = V_0 = \frac{4}{3}\pi R^3$ and $S_p = \pi R^2$.

We re-write this equation in a dimensionless form, dividing the LHS by the added-mass term :

$$-\frac{3}{2} \frac{f_{C,x}}{K^2 C_{AM,x1}} \frac{1}{Ca} \frac{Pr}{Ja_w^2} + \frac{1}{K^2 C_{AM,x1}} \frac{Re_b}{Fr} \frac{Pr}{Ja_w^2} + \frac{3}{8} \frac{C_D}{K^2 C_{AM,x1}} Re_b \frac{Pr}{Ja_w^2} + 1 = 0 \quad (4.134)$$

where we have the following non-dimensional numbers :

$$\begin{aligned} Re_b &= \frac{2RU_L}{\nu_L} ; \quad Fr = \frac{\rho_L U_L^2}{(\rho_L - \rho_V) gR} = Re_b^2 \frac{\rho_L \nu_L^2}{g (\rho_L - \rho_V) 4R^3} ; \quad We = \frac{\rho_L U_L^2 R}{\sigma} ; \quad Eo = \frac{(\rho_L - \rho_V) gR^2}{\sigma} \\ Ja_w &= \frac{(T_w - T_{sat}) \rho_L c_{p,L}}{\rho_V h_{LV}} ; \quad Pr = \frac{\nu_L}{\eta_L} ; \quad \frac{\dot{R}}{U_L} = \frac{K^2 Ja_w^2}{Pr Re_b} ; \quad Ca = \frac{\mu_L U_L}{\sigma} = Re_b \frac{\nu_L \mu_L}{2R \sigma} \end{aligned} \quad (4.135)$$

Since drag, added mass and buoyancy will promote detachment, we can derive criteria to compare each force's influence in the departure process :

$$\text{Added Mass greater than Drag if : } \frac{Ja_w^2}{Pr} > \frac{3}{8} \frac{C_D}{C_{AM,x1} K^2} \frac{1}{Re_b} \quad (4.136)$$

$$\text{Added Mass greater than Buoyancy if : } \frac{Ja_w^2}{Pr} > \frac{1}{C_{AM,x1} K^2} \frac{Re_b}{Fr} \quad (4.137)$$

$$\text{Drag greater than Buoyancy if : } Re_b > \frac{16}{3} C_D \frac{Eo}{Ca} = Re_c \quad (4.138)$$

We can then choose a diameter R and fluid properties to simultaneously plots those criteria on a $(Ja_w^2/Pr ; Re_b)$ map to visualize predominance ranges as shown on Figure 4.17.

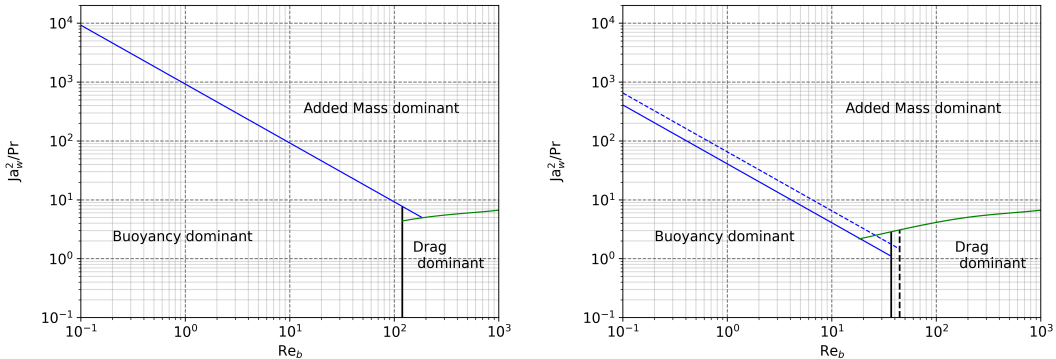


Figure 4.17: Force predominance map. Green, blue and black lines are respectively conditions (4.136), (4.137) and (4.138). Left represents $R = 0.25$ mm for water at 1 Bar. Right represents $R = 0.05$ mm, water at 150 Bar (plain lines) and R12 at 25 Bar (dashed lines).

It appears that the increase in pressure along with the bubble diameter decrease leads to a larger range of flow parameters for which added mass effects and drag will be dominant. In addition, we also plotted the conditions for R12 at the similarity pressure of 26 Bar where its properties such as We and ρ_L / ρ_V are close to water in PWR conditions [Garnier2001]. The proximity between the boundaries on Figure 4.17 interestingly indicates that *bubbles in pressurized R12 tests are likely to behave very similarly to bubbles in PWR regarding their departure by sliding*.

It is also interesting to note that the frontier between added mass and drag defined by condition (4.136) remains unchanged for the different pressures, fluids and bubble radii.

4.5.9 Application to Low Pressure Data

In order to apply the predominance criteria, we gathered three data sets of experimental bubble departure diameter measurements in vertical flow boiling of water at atmospheric pressure. The associated experimental conditions are gathered on Table 4.5.

Table 4.5: Thermal-hydraulics parameters range for the low pressure data.

Author	D_h (mm)	G (kg/m ² /s)	ΔT_w (K)	D_d (mm)	Re_b (-)	Ja_w^2/Pr
Sugrue <i>et al.</i> [Sugrue2014]	16.642	250 - 400	2 - 6	0.229 - 0.391	53.8 - 70.8	20.57 - 18
Guan <i>et al.</i> [Guan2014]	9	87.3 - 319.2	4.5 - 8.5	0.62 - 1.85	75.9 - 406.02	104.2 - 37
Maity [Maity2000]	20	0 - 239.6	5 - 5.9	0.788 - 1.713	0 - 241.04	128.6 - 17

To further justify the nearly-spherical shape hypothesis, we compute the range of Weber, Capillary and Eotvos numbers since they are representative of the deformability of the bubble under inertial, viscous and gravity effects (Table 4.6).

Table 4.6: Weber, Capillary and Eotvos numbers range for the low pressure data.

Author	We (-)	Ca (-)	Eo (-)
Sugrue <i>et al.</i> [Sugrue2014]	$6.36 \times 10^{-3} - 12.6 \times 10^{-3}$	$2.22 \times 10^{-4} - 3.64 \times 10^{-4}$	$2.09 \times 10^{-3} - 6.09 \times 10^{-3}$
Guan <i>et al.</i> [Guan2014]	$3.79 \times 10^{-3} - 82.8 \times 10^{-3}$	$0.998 \times 10^{-4} - 4.93 \times 10^{-4}$	$1.53 \times 10^{-2} - 13.6 \times 10^{-2}$
Maity [Maity2000]	$0 - 3.5 \times 10^{-2}$	$0 - 3.27 \times 10^{-4}$	$2.48 \times 10^{-2} - 11.7 \times 10^{-2}$

To compute the predominance boundaries as done in Figure 4.17, we need to choose a bubble radius. Here we take the average departure radius of each data set to plot the associated boundaries. It appears that Guan and Maity data sets have very close average departure radius (approx. 0.6 mm) and thus have the same predominance zones. The results are displayed on Figure 4.18.

It immediately appears that when departure by sliding occurs, 32 measurements out of 37 seem to be dominated by added mass effects. The remaining 5 are buoyancy-dominant (Guan and Maity data) but placed really close to the added mass / buoyancy boundary on the map. This observation tends to indicates that at low pressure and mass fluxes, the departure by sliding could be triggered mostly by the added mass effects resulting of the coupling between the rapid initial bubble growth and the surrounding liquid velocity (Subsection 4.1.6).

This is mainly a consequence of the significant wall superheat reached in such boiling conditions along with high values of ρ_L/ρ_V , leading to high values of Ja_w^2/Pr .

4.5.10 Application to High Pressure Data

Measurements of high-pressure bubble departure diameter are more difficult to find in the literature especially because of the great difficulty to provide clear visualization of individual bubbles when pressure increases, since bubbles are greatly reducing in size down to a few μm .

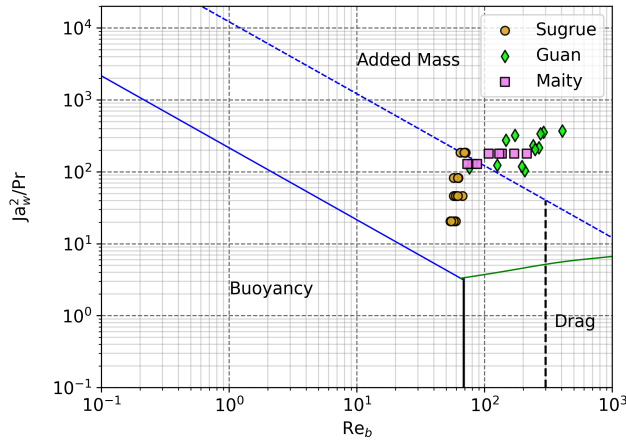


Figure 4.18: Experimental measurements in the dominance map. Plain lines correspond to Sugrue average departure radius (0.15 mm), dashed lines to Guan and Maity (0.59 mm).

Nevertheless, recent works such as those conducted by Kossolapov[Kossolapov2021] have managed to conduct such measurements at pressures up to 39.8 Bar. To evaluate the forces responsible for sliding at higher pressures, closer to PWR operating conditions, we conduct the same analysis as we did with the low-pressure data. Experimental operations and non-dimensional numbers are summed up in Table 4.7.

Table 4.7: Thermal-hydraulics parameters and dimensionless numbers range for Kossolapov data.

Author	D_h (mm)	G (kg/m ² /s)	P (Bar)	D_d (mm)	Re_b (-)
Kossolapov[Kossolapov2021]	11.78	500 - 2000	10.5 ; 19.9 ; 39.8	0.01 - 0.13	5.95 - 131.77
We (-)		Ca (-)		Eo (-)	
$0.5 \times 10^{-3} - 84.8 \times 10^{-3}$		$1.47 \times 10^{-4} - 14.8 \times 10^{-4}$		$0.82 \times 10^{-5} - 85 \times 10^{-5}$	

Wall superheat or heat flux values are not specified in Kossolapov data because the given diameters were used to depict a global trend with pressure and mass flux. However, wall superheat at **Onset of Nucleate Boiling** can be roughly estimated using Frost & Dzakowic correlation[Frost1967] which yields approximately $\Delta T_w \approx 4$ K for water at 40 Bar under a 1 MW/m² heat flux. To cover a tentatively large enough range of Ja_w^2/Pr values, we will place the measurements from Kossolapov on the predominance map assuming three possible wall superheats : 1 K, 5 K and 10 K.

The resulting map is displayed on Figure 4.19. In order to make it easier to interpret, we colored the stable added mass / drag boundary (4.136) in black and used 3 colors to distinguish between the three operating pressures. The arbitrary superheat are made distinct with the markers shapes.

The main observation here relates to the values of Ja_w^2/Pr which appear to be way smaller compared to the low pressure data, even for superheats as high as 10K. This is mainly resulting from the strong decrease in the ρ_L/ρ_V ratio with pressure, thus leading to predominance ranges where the force mostly responsible for departure by sliding is the drag. The higher

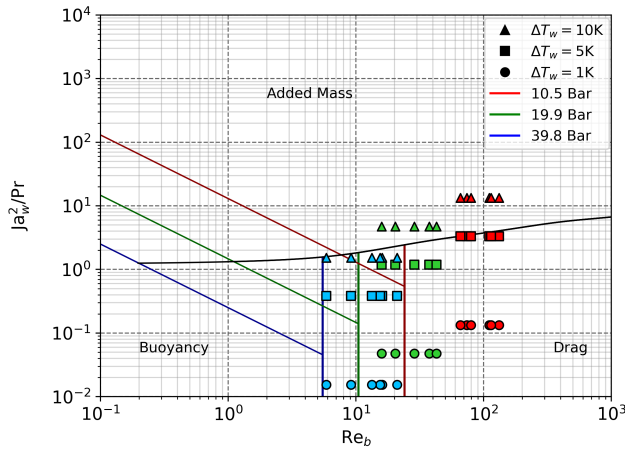


Figure 4.19: Experimental measurements from Kossolapov in the dominance map. Frontiers are plotted for the average departure radius at the given pressure. Blue : 39.8 Bar - Green : 19.9 Bar - Red : 10.5 Bar.

mass fluxes also tend to increase this effect. Added mass only start to be significant under the 10 K superheat assumption.

Finally, this analysis of high pressure data tends to indicate that departure by sliding at high pressure is triggered in significantly different dynamic conditions in term of forces ratio (drag dominant) compared to low pressure (added mass dominant).

4.6 PREDICTION OF BUBBLE DEPARTURE DIAMETER

The main goal of such a study would still remain to find a way to predict the departure diameter of bubbles in vertical flow boiling. Since only the capillary force is opposed to bubble departure, we can use non-dimensional force balance (4.134) to search the maximum diameter above which :

$$C_{AM,x} K^2 \frac{Ja_w^2}{\text{Pr}} + \frac{Re_b}{\text{Fr}} + \frac{3}{8} C_D Re_b > \frac{3}{2} \frac{f_{C,x}}{\text{Ca}} \quad (4.139)$$

To compute Re_b and C_D , we use Reichardt's law [Reichardt1951] for the wall liquid velocity and shear at a distance $y = R$. Diameters predictions results are displayed on Figure 4.20. The supposed wall superheat for Kossolapov data is 1 K.

We can see that the predicted diameters seem to reasonably follow the global trend with pressure, which is an important feature in order to distinguish the different dynamic regimes depending on the flow conditions.

The average contact and hysteresis angle used in the computations are $\theta = 45^\circ$, $d\theta = 36^\circ$ for Sugrue's data (maximum hysteresis observed in her experiments) yielding an average error of 230.4% ; $\theta = 53^\circ$, $d\theta = 27^\circ$ for Guan's data (maximum hysteresis measured, accounting for uncertainties) yielding an average error of 182% ; $\theta = 60^\circ$, $d\theta = 20^\circ$ for Maity's data (average static angle, but increased hysteresis compared to the measurements) for an average error of 29.2% ; $\theta = 45^\circ$, $d\theta = 1^\circ$ for Kossolapov's data for an average error of 53.8% (no measurements available).

Although the results seem to follow a correct trend with pressure, the average error can still be considered high on some data compared to other models [Klausner1993]. However, such models often chose arbitrary values for parameters like the bubble foot diameter ($d_w =$

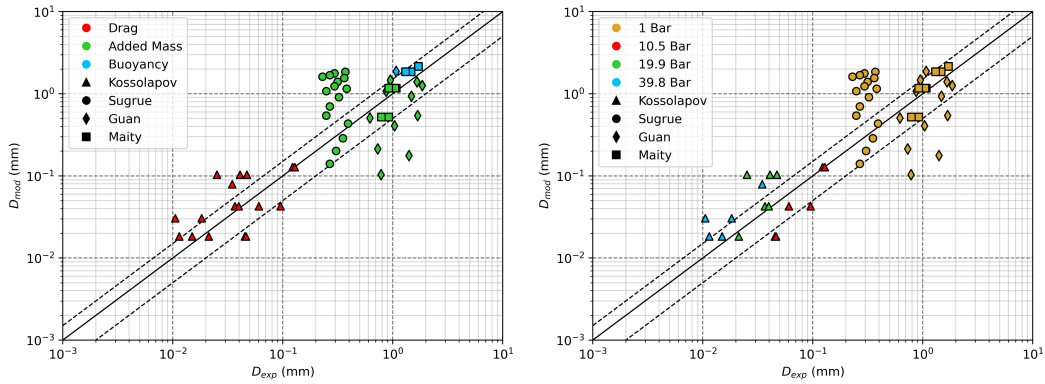


Figure 4.20: Predicted diameter by Eq. 4.139 vs. experimental measurements. Colors refer to the dominant force at the departure by sliding (left) or to the operating pressure (right). $\pm 50\%$ error lines in dashed black.

$D/15$) [Mazzocco2018] or the contact, hysteresis and inclination angles. Recent studies emphasized that such assumptions were substantially wrong [Bucci2021]. Moreover, those models consider an opposite contribution of the added mass regarding departure which seems to be incorrect as discussed earlier (Subsection 4.1.6).

In this work, we insisted on keeping straight assumptions of a quasi-spherical bubble and tried to apply the resulting laws for departure diameter prediction. **The only hypothetically free parameters were the average contact angle and hysteresis.** We tried to use author's data when available as inputs in our model. However, we did not have such measurements for Kossolapov's data and thus chose an average contact angle close to water FTO static contact angle (heater material used in his experiments) along with a very small hysteresis, since very small bubbles in highly pressurized flow will be likely to keep non-deformed shapes because of surface tension effects getting stronger as the bubble diminishes in size. Moreover, we had to set a wall superheat which we chose to be 1K (strongly drag-dominant regime).

Concerning the low pressure data, we observed that better results were obtained on Maity's measurements when using a bigger hysteresis angle. This may originate from the bubble foot diameter modeling, which was observed to be lower than the associated truncated sphere foot diameter in his experiments. In addition, the three low pressure data sets (Table 4.5) have very close flow conditions, but significantly different measured departure diameter, especially when comparing Sugrue to Guan and Maity. The observed differences in experimental measurements can thus originate from the heater material, which impact is only indirectly included through the contact angle and hysteresis. This can explain the over-estimation of departure diameter on Sugrue's data when good agreement is observed with Guan and Maity. The same goes for the under-estimated diameters on Guan's data when we have a good agreement with Sugrue's measurements, explaining the high average relative deviation on those data sets.

Part IV
TOWARDS THE INDUSTRIAL GEOMETRY

5

PROMOTEUR

5.1 BOILING FREON IN A TUBE WITH MIXING VANES : DEBORA-PROMOTEUR EXPERIMENTS

In this section, we simulate upward boiling flows of R12 in a vertical tube equipped with mixing vanes and compare the outlet void fraction profile predicted by NEPTUNE_CFD with measurements coming from the DEBORA-Promoteur experiment.

5.1.1 *Description of the experiment*

In 2003, the wish to investigate boiling flows in complex geometries similar to those in PWR fuel assembly lead CEA and EDF to modify the DEBORA facility to introduce mixing vanes (MV) within the tube. This mixing device has been designed to have the same geometric properties as the mixing vanes attached to rod bundle grids (Figure 5.1).

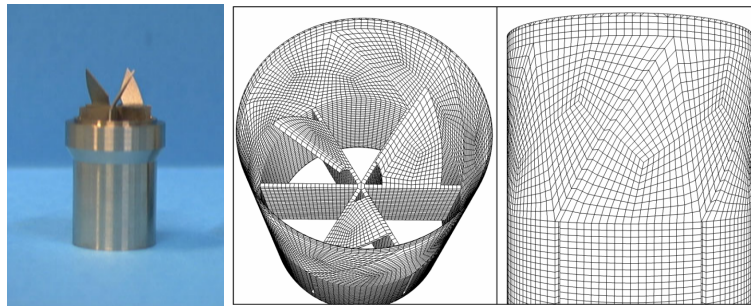


Figure 5.1: Picture of the mixing device (left) and its fine meshing (right).

Two series of measurements were conducted on this geometry :

- Campaign 4800 : measurements of α using two optical probes, mixing device placed $0.455m \approx 23.5D_h$ upstream the end of the heating length
- Campaign 5200 : measurements of α and $U_{G,z}$ using two optical probes, mixing device placed $0.192m \approx 10D_h$ upstream the end of the heating length

The goal of those tests was to observe the impact of the mixing device on the void fraction profile. The induced rotation is expected to gather the bubbles at the center of the tube and enhance condensation for highly subcooled cases. Those expectations are confirmed when looking at experimental α profiles on Figure 5.2. The strong differences compared to simple tube profiles could explain the gain on the CHF value in PWR thanks to the mixing grids. Cases are named following the same nomenclature as presented in Section 2.1.

5.1.2 NEPTUNE_CFD simulations of DEBORA-Promoteur cases

We simulated 3 cases for each position of the mixing device, covering different local thermodynamic quality near the vanes ($x_{eq,MV}$) :

- 48G3P26W23Te65 & 52G3P26W23Te65 with $x_{eq,MV} \approx -1\%$
- 48G3P26W23Te69 & 52G3P26W23Te69 with $x_{eq,MV} \approx 4\%$
- 48G3P26W23Te75 & 52G3P26W23Te75 with $x_{eq,MV} \approx 12\%$

Computations are conducted using two meshes for Te69 cases : a large one (M1) with 444 703 cells and a fine one (M2) with 3 487 627 cells. Results for void fraction profiles are shown on Figure 5.2.

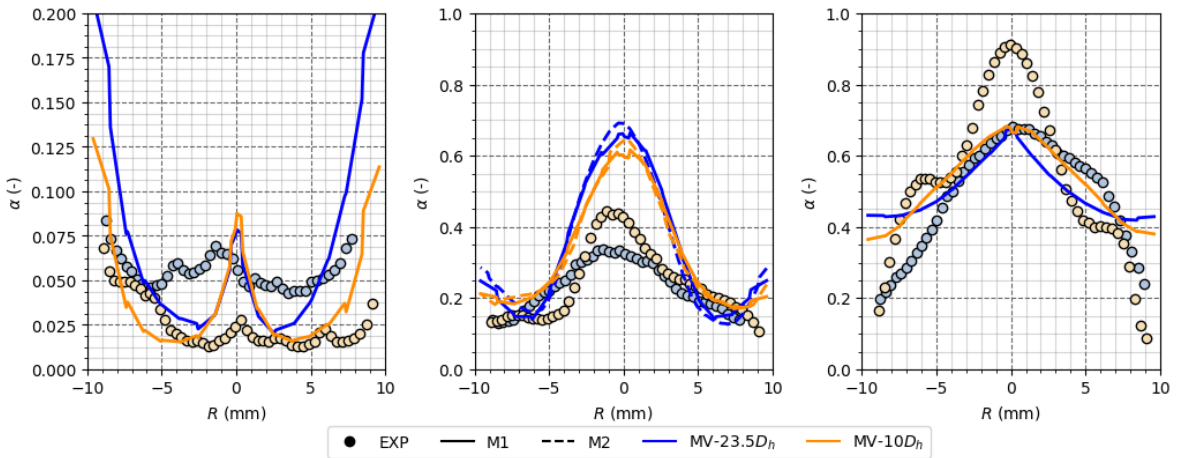


Figure 5.2: NCFD (lines) vs. Exp. (circles) - α profiles for two MV positions ($23.5D_h$ in blue, $10D_h$ in orange) - $T_{in} = 65^\circ\text{C}$ (left), $T_{in} = 69^\circ\text{C}$ (middle), $T_{in} = 75^\circ\text{C}$ (right) - Simulations using two meshes M1 (coarse) and M2 (fine) for $T_{in} = 69^\circ\text{C}$.

Quantitatively speaking, it seems that NEPTUNE_CFD reproduces the effect of vapor accumulation at the center thanks to the pressure gradient generated by the swirl induced by the mixing vanes. The radial position of the core void fraction peak correctly matches the experimental one.

However, measured void fraction profiles are not predicted correctly. A particularly strong overestimation of the core void fraction is observed as well as close to the wall. The CMFD results tend to rapidly reach a core void fraction around 60% ($T_{in} = 69^\circ\text{C}$ cases) and then flattens with increasing temperature ($T_{in} = 75^\circ$ cases). This contradicts experimental observation where the void fraction profile globally rises when inlet temperature increases, except at the wall where no peak is observed due to bubble removing effect by the liquid's rotation. Moreover, the $T_{in} = 75^\circ$ case with MV at $10D_h$ experimentally shows local α peaks at $R \approx \pm 6\text{mm}$ which remain currently unexplained and not reproduced by the simulations. To investigate what could be a potential origin for the core void fraction peak overestimation, we present in Section 5.2 single-phase flow simulations in the MV geometry.

5.2 LIQUID WATER FLOW IN A TUBE WITH MIXING VANES : AGATE-PROMOTEUR EXPERIMENT

In this penultimate section, we briefly investigate single-phase flow within the same geometry as Section 5.1.

5.2.1 Description of the experiment

In 2003, using the same experimental geometry as DEBORA-Promoteur cases (Section 5.1), Laser Doppler Velocimetry (LDV) measurements of velocity and turbulent fluctuations for an adiabatic single-phase flow of water were conducted. The outlet pressure was around $P = 2$ bar with an inlet mass flux $G \approx 3000 \text{ kg/m}^2/\text{s}$. Measurements were conducted on 6 different diameters and repeated at various axial positions upstream and downstream the mixing vanes.

A first look at experimental measurements (Figure 5.3) shows that the vanes geometry induces significantly non-symmetric velocity profile. Moreover, we observe high turbulent fluctuations which maximum is located at the same radial position as the maximum radial velocity gradient.

5.2.2 NEPTUNE_CFD simulations of AGATE-Promoteur case

On Figure 5.3, we present some of the results obtained with NEPTUNE_CFD using the $R_{ij} - \varepsilon$ SSG turbulence model on the M2 mesh, along with a smooth wall law and a rough wall law (roughness $\epsilon = 0.01\text{mm}$). The turbulent fluctuations Root Mean Square (RMS) correspond, for instance, to $\sqrt{\langle u_x'^2 \rangle}$ for the x direction where u_i' represents the fluctuating part of the velocity along component i and $\langle \cdot \rangle$ the time-averaging operator. Subscripts R and A stand for radial and axial values ; U_0 is the average inlet velocity.

Non-symmetric radial velocity profiles close to the MV are quite well reproduced by the simulations. However, far downstream the MV, it appears that the fluid's rotation is overestimated by the model with a smooth wall approach, while applying a roughness helps to reduce the magnitude of the swirl. Moreover, the radial turbulent fluctuations are better estimated by the rough wall approach at $z = 440 \text{ mm}$.

On the other hand, it seems that the rough wall approach deteriorates the axial velocity profile compared to the experiment. As shown on the bottom part of Figure 5.3, the smooth wall simulation returns a flat velocity profile closer to the experiment than the rough wall one which overestimates the core velocity peak.

Both simulations globally underestimate the turbulent fluctuations, which can have a significant influence over the observed discrepancies on velocity profiles since turbulence plays a key role to homogenize the fluid flow.

Those results finally highlight the fact that simulation of such rotating flows may need a particular wall approach to better capture the induced swirl and its dissipation. Correct prediction of turbulent fluctuations would be of significant interest to ensure liquid velocity validation. Further investigations on boiling cases could possibly be improved by a roughness approach, which is the current correction used for two-phase wall laws (Subsection 1.1.6).

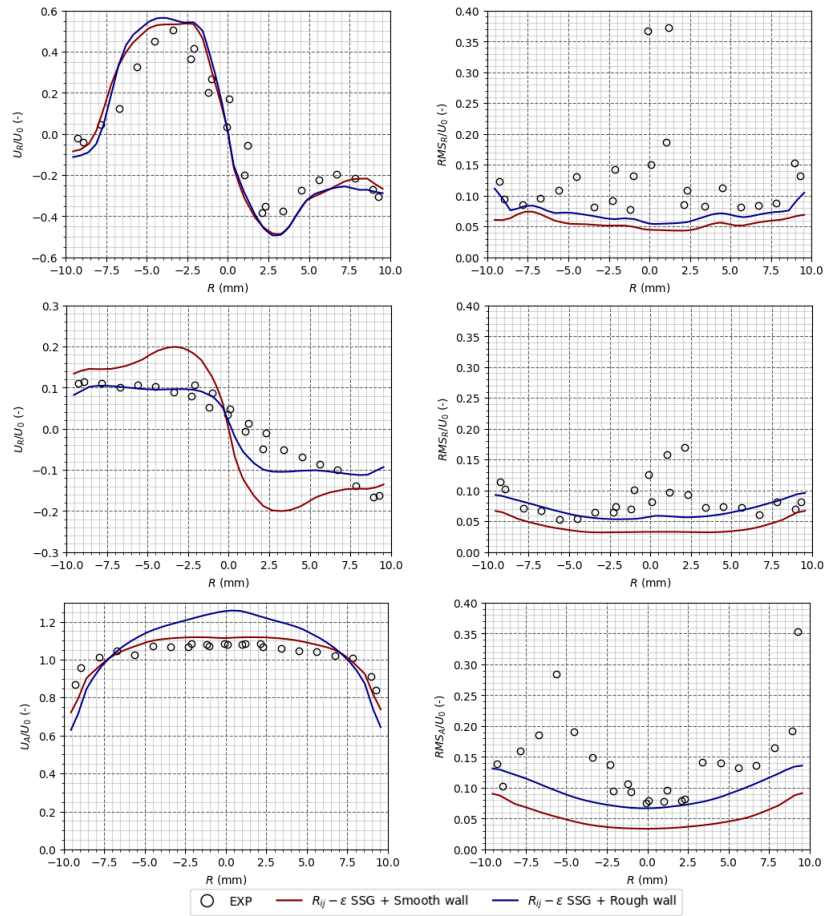


Figure 5.3: NCFD vs. Exp. - Top & Middle : Radial velocity and turbulent RMS ($z = 30\text{mm}$ & $z = 440\text{mm}$) - Bottom : Axial velocity and turbulent RMS ($z = 440\text{mm}$).

Part V
APPENDIX

A

DETAILS ON THE BUBBLE FORCE BALANCE

Aliquam lectus. Vivamus leo. Quisque ornare tellus ullamcorper nulla. Mauris porttitor pharetra tortor. Sed fringilla justo sed mauris. Mauris tellus. Sed non leo. Nullam elementum, magna in cursus sodales, augue est scelerisque sapien, venenatis congue nulla arcu et pede. Ut suscipit enim vel sapien. Donec congue. Maecenas urna mi, suscipit in, placerat ut, vestibulum ut, massa. Fusce ultrices nulla et nisl.

Etiam ac leo a risus tristique nonummy. Donec dignissim tincidunt nulla. Vestibulum rhoncus molestie odio. Sed lobortis, justo et pretium lobortis, mauris turpis condimentum augue, nec ultricies nibh arcu pretium enim. Nunc purus neque, placerat id, imperdiet sed, pellentesque nec, nisl. Vestibulum imperdiet neque non sem accumsan laoreet. In hac habitasse platea dictumst. Etiam condimentum facilisis libero. Suspendisse in elit quis nisl aliquam dapibus. Pellentesque auctor sapien. Sed egestas sapien nec lectus. Pellentesque vel dui vel neque bibendum viverra. Aliquam porttitor nisl nec pede. Proin mattis libero vel turpis. Donec rutrum mauris et libero. Proin euismod porta felis. Nam lobortis, metus quis elementum commodo, nunc lectus elementum mauris, eget vulputate ligula tellus eu neque. Vivamus eu dolor.

$$r_w = \frac{1}{2} (\sin(\theta_d) R + \sin(\theta_u) R) \quad (\text{A.1})$$

$$= \frac{R}{2} (\sin(\theta_s + d\theta) + \sin(\theta - d\theta)) \quad (\text{A.2})$$

$$= \frac{R}{2} \left[2\sin\left(\frac{\theta_s + d\theta + \theta_s - d\theta}{2}\right) \cos\left(\frac{\theta_s + d\theta - (\theta_s - d\theta)}{2}\right) \right] \quad (\text{A.3})$$

$$= R\sin(\theta_s) \cos(d\theta) \quad (\text{A.4})$$

$$\overline{F_{CP}} = \frac{2\sigma}{R_c} \frac{\pi d_w^2}{4} \overline{e_y} \quad (\text{A.5})$$

$$= \frac{2\sigma}{R} \frac{\pi 4R^2}{4} \sin^2(\theta) \cos^2(d\theta) \overline{e_\perp} \quad (\text{A.6})$$

$$= 2\sigma\pi R \underbrace{\sin^2(\theta) \cos^2(d\theta)}_{f_{cp}} \overline{e_\perp} \quad (\text{A.7})$$

$$= 2\pi R\sigma f_{cp}(\theta, d\theta) \overline{e_\perp} \quad (\text{A.8})$$

$$\overline{F_{CP}} \cdot \overline{e_\perp} = -d_w \sigma \frac{\pi}{\alpha_r - \alpha_u} (\cos(\alpha_a) - \cos(\alpha_r)) \quad (\text{A.9})$$

$$= \pi 2R \sigma \frac{\sin(\alpha + d\alpha) + \sin(\alpha - d\alpha)}{2} \frac{\cos(\alpha + d\alpha) - \cos(\alpha - d\alpha)}{2d\alpha} \quad (\text{A.10})$$

$$= 2\pi R \sigma \frac{2\sin(\alpha) \cos(d\alpha)}{2} \frac{(-2\sin(\alpha) \sin(d\alpha))}{2d\alpha} \quad (\text{A.11})$$

$$= -2\pi R \sigma \sin^2(\alpha) \underbrace{\frac{\sin(2d\alpha)}{2d\alpha}}_{f_{s,\perp}} \quad (\text{A.12})$$

$$= -2\pi R \sigma f_{s,\perp}(\alpha, d\alpha) \quad (\text{A.13})$$

$$(\text{A.14})$$

$$\overline{F_s} \cdot \overline{e_\parallel} = -1.215 d_w \sigma \frac{\pi(\alpha_r - \alpha_u)}{\pi^2 - (\alpha_r - \alpha_u)^2} (\sin(\alpha_r) + \sin(\alpha_u)) \quad (\text{A.15})$$

$$= -1.215 d_w \sigma \frac{\pi 2d\alpha}{\pi^2 - 4d\alpha^2} (\sin(\alpha + d\alpha) + \sin(\alpha - d\alpha)) \quad (\text{A.16})$$

$$= -1.215 2R \sigma \frac{\pi d\alpha}{\pi^2 - 4d\alpha^2} (\sin(\alpha + d\alpha) + \sin(\alpha - d\alpha))^2 \quad (\text{A.17})$$

$$= -2\pi R \sigma \frac{1.215 d\alpha}{\pi^2 - 4d\alpha^2} 4\sin^2(\alpha) \cos^2(d\alpha) \quad (\text{A.18})$$

$$= -2\pi R \sigma \underbrace{1.215 \frac{d\alpha}{(\frac{\pi}{2})^2 - d\alpha^2} \sin^2(\alpha) \cos^2(d\alpha)}_{f_{s,\parallel}} \quad (\text{A.19})$$

$$= -2\pi R \sigma f_{s,\parallel}(\alpha, d\alpha) \quad (\text{A.20})$$

A.1 APPENDIX SECTION TEST

Nulla in ipsum. Praesent eros nulla, congue vitae, euismod ut, commodo a, wisi. Pellentesque habitant morbi tristique senectus et netus et malesuada fames ac turpis egestas. Aenean nonummy magna non leo. Sed felis erat, ullamcorper in, dictum non, ultricies ut, lectus. Proin vel arcu a odio lobortis euismod. Vestibulum ante ipsum primis in faucibus orci luctus et ultrices posuere cubilia Curae; Proin ut est. Aliquam odio. Pellentesque massa turpis, cursus eu, euismod nec, tempor congue, nulla. Duis viverra gravida mauris. Cras tincidunt. Curabitur eros ligula, varius ut, pulvinar in, cursus faucibus, augue.

Nulla mattis luctus nulla. Duis commodo velit at leo. Aliquam vulputate magna et leo. Nam vestibulum ullamcorper leo. Vestibulum condimentum rutrum mauris. Donec id mauris. Morbi molestie justo et pede. Vivamus eget turpis sed nisl cursus tempor. Curabitur mollis sapien condimentum nunc. In wisi nisl, malesuada at, dignissim sit amet, lobortis in, odio. Aenean consequat arcu a ante. Pellentesque porta elit sit amet orci. Etiam at turpis nec elit ultricies imperdiet. Nulla facilisi. In hac habitasse platea dictumst. Suspendisse viverra aliquam risus. Nullam pede justo, molestie nonummy, scelerisque eu, facilisis vel, arcu.

A.2 ANOTHER APPENDIX SECTION TEST

Curabitur tellus magna, porttitor a, commodo a, commodo in, tortor. Donec interdum. Praesent scelerisque. Maecenas posuere sodales odio. Vivamus metus lacus, varius quis, imperdiet quis, rhoncus a, turpis. Etiam ligula arcu, elementum a, venenatis quis, sollicitudin sed, metus. Donec nunc pede, tincidunt in, venenatis vitae, faucibus vel, nibh. Pellentesque wisi.

LABITUR BONORUM PRI NO	QUE VISTA	HUMAN
fastidii ea ius	germano	demonstratea
suscipit instructior	titulo	personas
quaestio philosophia	facto	demonstrated

Table A.1: Autem usu id.

Nullam malesuada. Morbi ut tellus ut pede tincidunt porta. Lorem ipsum dolor sit amet, consectetur adipiscing elit. Etiam congue neque id dolor.

Donec et nisl at wisi luctus bibendum. Nam interdum tellus ac libero. Sed sem justo, laoreet vitae, fringilla at, adipiscing ut, nibh. Maecenas non sem quis tortor eleifend fermentum. Etiam id tortor ac mauris porta vulputate. Integer porta neque vitae massa. Maecenas tempus libero a libero posuere dictum. Vestibulum ante ipsum primis in faucibus orci luctus et ultrices posuere cubilia Curae; Aenean quis mauris sed elit commodo placerat. Class aptent taciti sociosqu ad litora torquent per conubia nostra, per inceptos hymenaeos. Vivamus rhoncus tincidunt libero. Etiam elementum pretium justo. Vivamus est. Morbi a tellus eget pede tristique commodo. Nulla nisl. Vestibulum sed nisl eu sapien cursus rutrum.

There is also a useless Pascal listing below: [Listing A.1](#).

Listing A.1: A floating example (`listings` manual)

```

1 for i:=maxint downto 0 do
begin
{ do nothing }
end;
```

DECLARATION

Put your declaration here.

Paris, December 2022

Luc Favre

COLOPHON

This document was typeset using the typographical look-and-feel **classicthesis** developed by André Miede. The style was inspired by Robert Bringhurst's seminal book on typography "The Elements of Typographic Style". **classicthesis** is available for both L^AT_EX and L_YX:

<https://bitbucket.org/amiede/classicthesis/>

Happy users of **classicthesis** usually send a real postcard to the author, a collection of postcards received so far is featured here:

<http://postcards.miede.de/>